1 **W-band S/Z Relationships for Rimed Snow Particles: Observational Evidence from**

2 **Combined Airborne and Ground-based Observations**

4 Shelby Fuller [1], Sam Marlow [1], Samuel Haimov [1], Matthew Burkhart [1], Kevin Shaffer [1], Austin

5 Morgan [1], and Jefferson R. Snider [1,2]

7 [1] Department of Atmospheric Science, University of Wyoming, Laramie, WY, USA
8
9
10
11 [2] Corresponding Author, jsnider@uwyo.edu

Abstract

Values of undercatch-corrected liquid-equivalent snowfall rate (S) at a ground site and microwave reflectivity (Z) retrieved using an airborne W-band radar were acquired during overflights. The temperature at the ground site was between -6 and -15 ^{o}C. At flight level, within clouds containing ice and supercooled liquid water, the temperature was approximately 7 ^{o}C colder. Additionally, airborne measurements of snow particle imagery were acquired. The images demonstrate that most of the snow particles were rimed, at least a flight level. A relatively small set of S/Z pairs (4) are available from the overflights. Important distinctions between these measurements and those of Pokharel and Vali (2011), who ~~also~~ reported ~~W-band~~ S/Z pairs and an S/Z relationship for rimed snow particles, are 1) the fewer number of S/Z pairs, 2) the method used to acquire S, and 3) the altitude, relative to ground, of the W-band Z retrievals. This analysis corroborates that the S/Z relationship reported in Pokharel and Vali (2011) yields an S - in scenarios with snowfall produced by riming - substantially larger than that derived using an S/Z relationship developed for unrimed snow particles.

~~This analysis indicates that the S/Z relationship reported in Pokharel and Vali (2011) yields an S, in scenarios with snowfall produced by riming, that is substantially larger than that derived using an S/Z relationship developed for unrimed snow particles.~~

1 - Introduction

32   Improvement of methods used to measure snowfall and rainfall are an ongoing focus of

33   meteorological research. The various methods are ground-based instruments that evaluate the

34   mass of precipitation that falls into or onto a collector (precipitation gauges) (Brock and

35   Richardson 2001), ground-based radars (Wilson and Brandes 1979), and airborne and space-

36   borne radars (Matrosov 2007; Kulie and Bennartz 2009; Geerts et al. 2010; Skofronick-Jackson

37   et al. 2017). An objective of these approaches, whether used to make observations independent

38   of other methods (e.g., Kulie and Bennartz 2009), or as a component of multiple observations

39   (e.g., Cocks et al. 2016), is estimation of precipitation rate and accumulated~~ion~~ precipitation

40   amount~~.~~

41   Many studies have investigated using radar for evaluating rainfall (for a review see

42   Wilson and Brandes 1979). There are two approaches. The first is research, both observational

43   and computational, that probes the relationship between rainfall rate (R) and radar-measured

44   values of range-corrected backscattered microwave power. The latter is commonly reported as an

45   equivalent radar reflectivity factor (Z_e). The second is operational in the sense that precipitation

46   gauges are used to calibrate measurements acquired using weather surveillance radars.

47   Complications associated with converting Z_e to R, or converting a radar reflectivity factor[1] (Z) to

48   R, can be grouped in four categories: 1) Inaccuracy in quantification of Z, 2) variation of the

49   R/Z relationship stemming from precipitation processes (e.g., coalescence and break up), 3)

50   difference between the volume of a radar range gate versus the much smaller volume of

---

[1] Radars are calibrated to report Z_e (Smith 1984). Herein, radar reflectivities are reported as $Z = Z_e$ and as dBZ = $10\log_{10}(Z_e)$.

51   atmosphere sampled as precipitation falls to a gauge, and 4) vertical displacement between a

52   radar range gate and a calibrating gauge, especially at far ranges.

53   For situations with snowfall, methods employing either gauge or radar are associated

54   with complications beyond that incurred in rainfall (Matrosov 2007; Martinaitis et al. 2015;

55   Cocks et al. 2016). Problems associated with gauge measurements are wind-induced snow

56   particle undercatch, gauge capping, delayed registration, and blowing snow aliasing as snowfall.

57   Moreover, in a a situation with snow particles more most abundant within a radar range gate,

58   compared to rain drops, and where a measurement of Z is used to infer R via a R/Z relationship,

59   the resultant precipitation rate will likely be inaccurate. This is because hydrometeor shape,

60   density, and dielectric properties are all variable for snow particles while relatively invariant for

61   rain drops. Additionally, a snow particle's terminal fall speed varies with size (as is the case for

62   drops) and with particle shape and particle density. Going forward, we refer to the latter two

63   properties as shape and density.

64   The goals of this paper are as follows: 1) to describe measurements of undercatch-

65   corrected liquid-equivalent snowfall rate (S, mm h^{-1}) and how these were paired with W-band

66   measurements of reflectivity (Z, mm^6 m^{-3}) ; 2) to contrast the S/Z pairs against S/Z relationships

67   commonly applied in radar retrievals of S; and 3) to investigate why the S/Z pairs deviate from

68   predictions of some S/Z relationships.

69   In calculations of paired values of S and Z, density is an important parameter. Density is

70   commonly estimated using empirical data (e.g., Pokharel and Vali 2011, [PV11]). For graupel, a

71   snow particle that grows via collection of supercooled cloud droplets in a process commonly

72   referred to as riming, paired observations of particle mass and particle size have been used to

73   estimate density. There is considerable uncertainty in this approach. Based on data collected at

74   two northwestern US surface sites (Zikmunda and Vali 1972; Locatelli and Hobbs 1974), density

75   values differ by at least a factor of two at particle sizes smaller than 2000 μm (PV11; their Fig.

76   4). Given that the density of rime ice varies with droplet impact speed, droplet size, and

77   temperature (Macklin 1962), it is not surprising that the density-size relationships analyzed by

78   PV11 are so varied.

79   Table 1 and the ~~he~~ following ~~introductory~~ paragraphs overview W-band S/Z relationships

80   ~~being~~ applied in instances with snow particles grown~~of snowfall where mass is acquired~~ by

81   vapor deposition (crystal), by collection of crystals (aggregate snowflake), and by riming (rimed

82   crystal and graupel). Henceforth, the latter two snow particle types are collectively referred to as

83   rimed snow particles.

84   In a computational study, Hiley et al. (2011) considered a variety of snow particle types

85   (column, plate, bullet rosette, sector plate, dendrite, and aggregate snowflake), employed a

86   parameterized ice particle size distribution (PSD) function (Field et al. 2005), accounted for a

87   range of temperature (-5 to -15 °C) via the Field et al. parameterization, and developed a range of

88   S/Z relationships for snow particles. Except for the aggregate snowflakes (henceforth,

89   aggregates)~~s~~, the modeled particle types were vapor-grown crystals. Hiley et al.'s upper- and

90   lower-limit relationships are $S = 0.21 \cdot Z^{0.77}$ and $S = 0.024 \cdot Z^{0.91}$, respectively. ~~—~~Matrosov (2007)

91   developed an S/Z relationship for aggregates. In that work, parameterized PSDs from Braham

92   (1990) were employed, and a range of particle aspect ratios were factored into the calculations.

93   For aggregates, the S/Z relationship is $S = 0.056 \cdot Z^{1.25}$ (Matrosov 2007). It should be noted that

94   Hiley et al. (2011) and Matrosov (2007) employed similar, but not identical, computational

95   methods. Computational research was also conducted by Kulie and Bennartz (2009) who

96   ~~developed~~ adopted t~~an S/Z relationship for what they referred to as a "snow particle" type. T~~he

97   wavelength-dependent density derived by Surussavadee and Staelin (2007) (200 kg m^{-3} at $\lambda =$

98   3.2 mm), modeled the ~~was adopted, the~~ snow particles ~~were modeled~~ as spheres, and applied

99   PSDs based on~~the~~ Field et al. ~~parameterization was applied~~. The resultant S/Z ~~relationship~~

100   ~~developed for this particle type~~ is S = 0.52·Z$^{0.83}$ (Surussavadee and Staelin 2007; Kulie and

101   Bennartz 2009; henceforth, SSKB). Variance in the calculations discussed in this paragraph

102   originate from changes in density, shape, fall speed, PSD, and particle size as these changes are

103   propagated through the cloud-microphysical and microwave-scattering calculations.

104   In a hybrid approach (computational and an analysis of measurements~~airborne~~

105   ~~observations~~), PV11 concluded that most of the snow particles they imaged were rimed snow

106   particles. Values of S were calculated using a density-size function (ρ_1, discussed below), a fall

107   speed-size function, ~~a~~ measured PSDs and measured particle images, and a determination of

108   particle volumes. It was assumed that a prolate spheroid approximated particle shape and that

109   shape ~~is~~ was the basis for determining a particle's sphere-equivalent volume and the particle's

110   sphere-equivalent size. The sphere-equivalent size was applied in the two functions. Values of Z

111   were calculated using a measured PSD, sphere-equivalent sizes, the ρ_1 function, and Mie Theory.

112   PV11 presented calculations of Z, obtained using two density-size relationships (their Eqs. 1 and

113   2) and compared their calculated reflectivities to measurements of Z from a W-band radar. That

114   led to their conclusion that "...the lower density assumption…yielded closer correspondence to

115   observed reflectivities." Their recommendation for S as a function of measured Z - hereafter the

116   S(ρ_1)/Z best-fit line - is S = 0.39·Z$^{0.58}$. Values of Z that were paired with the calculated values of

117   S (i.e., the S/Z pairs from PV11 that we present in Sect. 4), and that were used to determine the

118   S(ρ_1)/Z best-fit line, came from the WCR. In addition to variance in their values of S, coming

119   from a dependence on density, PV11 state that a value of S derived via their best-fit line is

120 uncertain by a factor-of-ten. That uncertainty is evident in the variance of S/Z data pairs about

121 the S(ρ_1)/Z line in Fig. 11 of PV11. Those investigators, and Geerts et al. (2010), attributed the

122 variance to use of two-dimensional snow particle images in calculations of S and to actual

123 variations of density, shape, and particle size not accounted for in the calculations.

124 A~~lso relevant are~~nother set of hybrid-type S/Z relationships was developed~~reported~~ by

125 Falconi et al. (2018; their Table 2). These are based on~~were developed using~~ measurements from

126 a video disdrometer, weighing precipitation gauge, microwave radiometer, and a vertically-

127 pointing W-band radar. All these systems were operated at the ground. The data set was stratified

128 into intervals of lightly-rimed, moderately-rimed, and heavily-rimed snow. A proxy for snow

129 particle riming - radiometer measurements of liquid water path – was the basis for the

130 stratifications (von Lerber et al. 2017). The S/Z relationships are $S = 0.10 \cdot Z^{1.0}$ (lightly-rimed), S

131 $= 0.079 \cdot Z^{1.3}$ (moderately-rimed), and $S = 0.060 \cdot Z^{1.4}$ (heavily-rimed).

132 Our focus is on surface measurements of S and on pairing of those measurements with

133 airborne measurements of Z. We also analyze airborne measurements of snow particle imagery.

134 The latter demonstrate~~s~~ that the particles observed at flight level were rimed. The imagery is the

135 ~~se measurements are the~~ basis for our assertion that our data set is relevant to ongoing

136 investigations of using Z to evaluate S in situations where precipitation is produced by riming.

137 Section 2 describes the setting of our study, the instruments we deployed, and recordings

138 we obtained using two data acquisition systems. One of the data systems was operated at a

139 ground site and the other on an aircraft. Section 3 is an analysis of the recordings; this section

140 also considers recordings from two additional, but ancillary, ground sites. Our findings are

141 discussed in Sect. 4 and summarized in Sect. 5. An Appendix (Sect. 6) explains how we

142 averaged recordings of near-surface W-band reflectivities and surface-based recordings of

143 snowfall.

144 Table 1 – W-band S/Z relationships from the literature, snow particle type, and values of minimum relative S difference

Reference	Abbreviation used for reference	S/Z relationship	Snow Particle Type	Minimum relative S deference on December 15 2016 [a]	Minimum relative S difference on January 3 2017 [a]
Hiley et al. (2011)	-	$S=0.21 \cdot Z^{0.77}$	Upper-limit S/Z relationship for vapor-grown crystals	0.7	1.0
Matrosov (2007)	-	$S=0.056 \cdot Z^{1.2}$	Aggregates	1.4	8.5 [b]
Surussavadee and Staelin (2007) and Kulie and Bennartz (2009)	SSKB	$S=0.52 \cdot Z^{0.83}$	Spherical snow particles with density = 200 kg m^{-3}	0.3	0.2 [c]
Pokharel and Vali (2011)	PV11	$S=0.39 \cdot Z^{0.58}$	Rimed snow particles assuming the lower of two density-size relationships	0.3	0.0 [d]
Falconi et al. (2018)	-	$S=0.060 \cdot Z^{1.4}$	Snow particles classified as heavily rimed	0.6 [e]	8.5

145

146 [a] Minimum relative S difference is defined as the minimum of $|(S_{HP}-S)|/S$ where S_{HP} is a measurement of undercatch-corrected liquid-equivalent
147 snowfall rate (Table 6) and S is a snowfall rate on an S/Z relationship line evaluated at one of the attenuation-corrected reflectivities (Sect. 4).

148 [b] Attenuation-corrected Z on this day (0.6 mm^6 m^{-3}) is smaller than the lower-limit Z (1 mm^6 m^{-3}) advised for this S/Z relationship (Matrosov
149 2007).

150 [c] Maximum relative S difference on this day is 0.4.

151 [d] Maximum relative S difference on this day is 0.7.

152 [e] Maximum relative S difference on this day is 0.9.

153

154 **2 - Site, Aircraft, and Instruments**

155 **2.1 - Site**

156   Analyzed herein are aircraft and ground data from 14/15 December 2016 and from 3

157 January 2017. The ground data were acquired in a forest/prairie ecotone on the eastern slope of

158 the Medicine Bow Mountains in southeast Wyoming (Figs. 1a-b). No ground-based observers

159 were deployed during the two snowfall events analyzed.

160   At one of three ground sites (HP in Figs. 1a-b) a hotplate precipitation gauge (Rasmussen

161 et al. 2011; Zelasko et al. 2018), a GPS receiver, and a data acquisition system were deployed.

162 Once per second, the data system ingested a hotplate-generated data string, combined that with

163 time-of-day from the GPS receiver [Coordinated Universal Time (UTC)], and recorded the

164 merged hotplate/UTC data string. The absolute accuracy of the time stamp is no worse than 2 s.

165   Overflights of the hotplate were done by the University of Wyoming King Air (WKA) on

166 14/15 December 2016 and on 3 January 2017. The flights were conducted in preparation for the

167 SNOWIE field project (Tessendorf et al. 2019) and were flown from the Laramie, WY Airport

168 (LA in Fig. 1a). Data acquisition on the WKA was also synchronized with UTC, but with much

169 better accuracy than at the hotplate.

170

171   Measurements of horizontal wind (speed and direction), temperature, relative humidity,

172   and pressure from the US-GLE AmeriFlux tower (AF in Figs. 1a-b) are also components the

173   analysis. The AmeriFlux data were provided to us as 30-minute averages (AmeriFlux 2021;

174   Marlow et al. 2023).

175
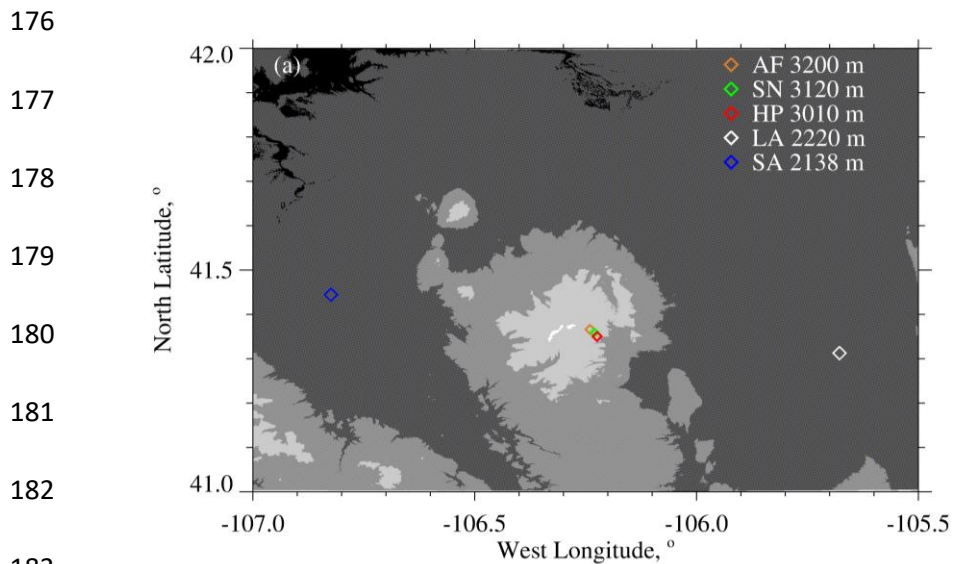
Figure 1 – (a) Southeast Wyoming, airport at Saratoga, WY (SA), airport at Laramie, WY (LA),

and the ground sites: AF = US-GLE AmeriFlux tower, SN = Brooklyn Lake SNOTEL, and HP =

hotplate. Altitudes of the airports and ground sites are in the legend. Altitude thresholds for the

digital elevation map are 1500, 2000, 2500, 3000, and 3500 meters. (b) Close up of the AF, SN,

and HP ground sites (from © Google Earth).

2.2 - University of Wyoming King Air (WKA)

The following WKA measurements were analyzed: aircraft position, temperature, snow particle imagery, and three moments of the cloud droplet size distribution function. A Cloud Droplet Probe (CDP; Faber et al. 2018) was the basis for the droplet size distribution measurements and the derived moments. The latter are droplet concentration (N), cloud liquid water content (LWC), and mean droplet diameter (<D>). Snow particle imagery was obtained using a precipitation particle imaging probe (2DP; Korolev et al. 2011) and a cloud particle imaging probe (2DS; Lawson et al. 2006). These acquired two-dimensional images of particles between 200 to 6400 μm (2DP) and between 10 to 1280 μm (2DS).

2.3 – The W-band Wyoming Cloud Radar (WCR)

Retrievals from the up-looking and down-looking antennas of the WCR, operated on the WKA, were also analyzed. For this we used Level 2 WCR data[2] with reflectivities recorded as $dBZ = 10 \cdot \log_{10}(Z)$. The reflectivities were converted from dBZ to Z prior to processing. Additionally, values of the vertical-component Doppler velocity retrieved from below the WKA using the WCR's down-looking antenna were analyzed. The Doppler velocities were corrected for aircraft motion as described in Haimov and Rodi (2013). We use V_D to symbolize the corrected vertical-component Doppler velocity and adopt the convention that $V_D > 0$ indicates upward hydrometeor motion.

---

[2] http://flights.uwyo.edu/uwka/wcr/projects/snowie17/PROCESSED_DATA/

217   The Level 2 WCR sampling was different on the two flight days and this difference is

218   shown in Table 2~~1~~. Ground-based calibrations of the WCR's up-looking antenna and correlations

219   between in-flight retrievals acquired using the WCR's up-looking and down-looking antennas

220   were used to estimate the precision and absolute accuracy of the WCR-derived values of dBZ.

221   These are $\pm$ 1.0 dBZ and $\pm$ 2.5 dBZ, respectively (PV11).

222

223   Table 2~~1~~ – Level 2 WCR sampling and the WKA overflight time

224

Date	Level 2 WCR Vertical Sampling, m	Level 2 WCR Along-track Sampling, s	Overflight Time, UTC
14/15 December 2016	23	0.23	00:00:38 (15 December 2016)
3 January 2017	30	0.36	20:32:03

225
226

2.4 - Hotplate Gauge

Algorithms used to process hotplate measurements are described in Rasmussen et al. (2011), Boudala et al. (2014), and Zelasko et al. (2018). Henceforth, these are referred to as R11, B14, and Z18, respectively. This section describes how hotplate measurements acquired at the HP site were analyzed. The hotplate deployed at the HP site is described in Wolfe and Snider (2012), Z18, and in Marlow et al. (2023).

Five measurements fundamental to the steady state energy budget of the hotplate's temperature-controlled up-viewing plate are output by the hotplate microprocessor as one-minute running averages (Z18). These averages were merged with the GPS time and recorded at 1 Hz by the data acquisition system (Sect. 2.1). With these measurements, calibration data (Marlow et al. 2023), and the algorithm developed by Z18, we calculated S in two steps. First, the five hotplate measurements (electrical power supplied to the plate, ambient temperature, wind speed, downwelling shortwave flux, and downwelling longwave flux) were input to Eq. 3 in Z18. The output of that equation is a provisional liquid-equivalent precipitation rate. Second, the snow particle catch efficiency, described in the next paragraph, was used to calculate S as the ratio of the provisional rate and the catch efficiency.

Marlow et al. (2023; their Fig. 3b) report the relationship between snow particle catch efficiency and wind speed that was applied in the calculation of S. There are three bases for this relationship. First is the catch efficiencies R11 derived using measurements obtained from a weighing gauge, operated within a double fence intercomparison reference shield, and collocated measurements from an unshielded hotplate gauge. These paired measurements are symbolized SRG (shielded reference gauge) and UHG (unshielded hotplate gauge). R11 plotted hotplate catch efficiencies (i.e., UHG/SRG) versus wind speeds measured at 10 m AGL (their Fig. 8).

250   Second is Marlow et al.'s adjustment of R11's 10 m AGL wind speeds to 2 m AGL. The basis

251   for the adjustment is surface boundary layer parameters derived for R11's site (Kochendorfer et

252   al. 2018) and an equation from Panofsky and Dutton (1984; their Eq. 6.7). The adjustment was

253   made because the hotplate-derived wind speeds, both here and in Marlow et al. (2023), were

254   acquired at approximately 2 m above the snowpack surface. Third is Marlow et al.'s comparison

255   of SNOTEL-derived liquid-equivalent depth changes and hotplate-derived time-integrated

256   accumulations. The interval for the comparisons is 24 hours. Based on the comparison, which

257   has 57 paired values acquired at the sites labeled HP and SN in Fig. 1, the average fractional

258   absolute relative difference is 0.30. Marlow et al. also provided an estimate of the error in a

259   SNOTEL measurement (2.4 mm). At accumulation = 10 mm the error corresponds to a relative

260   error = 0.24. This indicates that SNOTEL contributed significantly to the SNOTEL/hotplate

261   variance and especially so for the smaller accumulations in Fig. 9a of Marlow et al. (2023).

262   Because of this, we do not limit the following estimate of hotplate precision to a subset of the 57

263   paired measurements. Based on our assessment of the average fractional absolute relative

264   difference, the hotplate precision applied in this analysis was taken to be 0.3.

265   The hotplate-derived wind speeds acquired at ~ 2 m, and discussed in the previous

266   paragraph, are henceforth symbolized U_{PRO}. The basis for these is a steady state energy budget of

267   the hotplate's temperature-controlled down-viewing plate and a proprietary algorithm (R11 and

268   Z18). The U_{PRO} are reported by a hotplate as one-minute running averages (Z18) and we

269   recorded these at 1 Hz. Examples are the gray dots in Fig. 2. Additionally, we calculated and

270   analyzed one-minute-averaged values of U_{PRO} and the corresponding standard deviations.

271   Examples of these are the black circles and the short vertical line segments in Fig. 2.

272
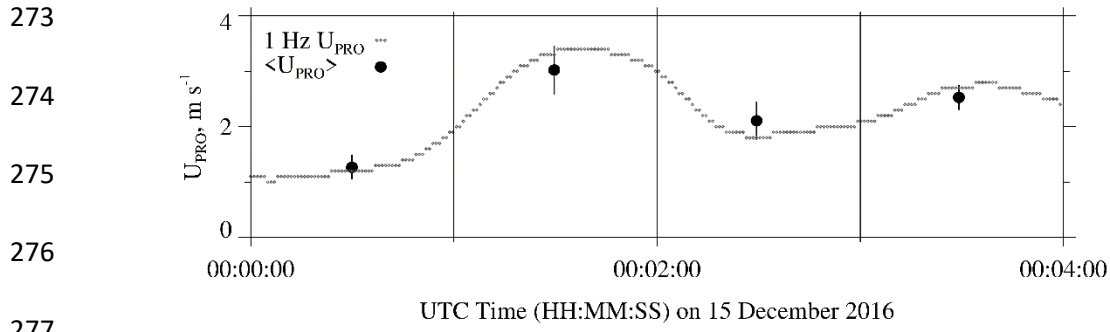
Figure 2 – Hotplate wind speed measurements (U_{PRO}) 00:00:00 to 00:04:00 on 15 December 2016. Gray dots are the one-minute running-average U_{PRO} recorded at 1 Hz. Black circles are the one-minute-averaged U_{PRO} (± 1 standard deviation).

283   **3 - Analysis**

284   **3.1 - WKA Overflight Time**

285   The focus of our analysis is the two WKA flight segments shown in Figs. 3a-b. The maps

286   shown in the figures have the three ground sites (AF, SN, and HP) and the WKA flight tracks

287   (white line). The beginning-to-end time interval for the flight tracks is 100 s and these are

288   divided into ten 10-second intervals. The 10 s intervals are indicated with white diamonds.

289   Except for the turn evident in Fig. 3b, the flight tracks are straight, and the track direction is

290   approximately upwind to downwind.

291   Times that the WKA was closest to the HP site were evaluated by finding the point on the

292   flight track where the horizontal position of the WKA was closest to the hotplate's coordinates.

293   These times are symbolized t_0 and are referred to as overflight times. In Figs. 3a-b the downwind

294   end of the flight tracks end at the overflight time. The latitude/longitude position of the aircraft

295   was within 390 m of the hotplate at the overflight times. Table 21 has the overflight times on the

296   two flight days.

297

298

299

300

301

302

303

304
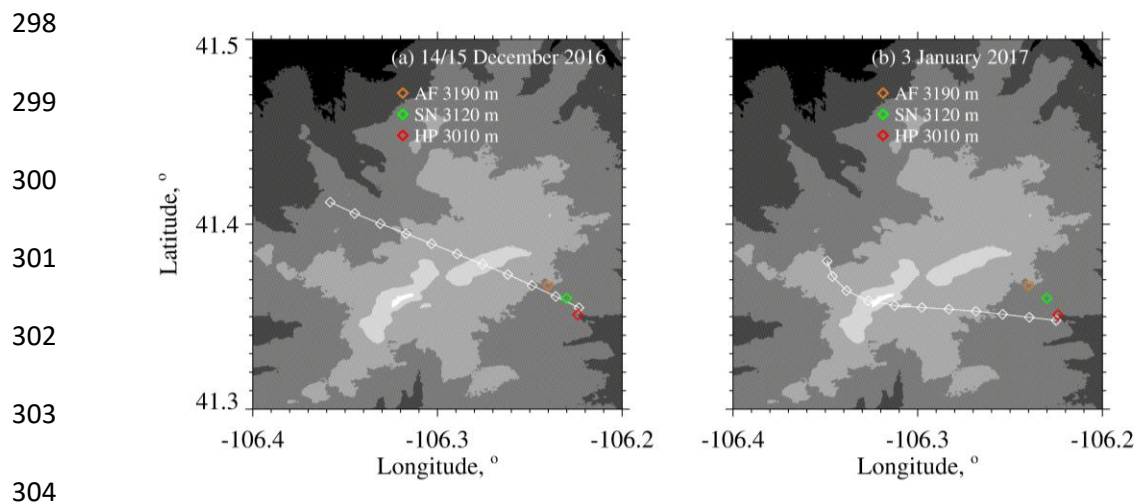
305 Figure 3 – (a) WKA flight track on 14/15 December 2016 for time interval = overflight time -

306 100 s to the overflight time. (b) WKA flight track on 3 January 2017 for time interval =

307 overflight time - 100 s to the overflight time. The white diamonds on the tracks are separated, in

308 time, by 10 s. Altitude thresholds for the digital elevation maps are 2600, 2800, 3000, 3200,

309 3400, and 3600 meters. Altitudes of the ground sites are in the legend.

310

311   **3.2 – Effect of Attenuation on WCR Reflectivities**

312

313   The presence of molecular oxygen, water vapor, cloud water, and snow particles within

314   the WCR's transmission path will contribute to an attenuation of microwave intensity and will

315   therefore negatively bias the retrieved reflectivities (Matrosov 2007; Hiley et al. 2011; Kneifel et

316   al. 2015). Models of attenuation, radar remote sensing, and in situ measurements were used to

317   calculate this bias. For oxygen, an attenuation coefficient from Ulaby et al. (1981; their Fig. 5.6),

318   and temperature (T) and pressure (P) measurements from the AF (Table 3~~2~~), were used. For

319   vapor, an attenuation coefficient (Ulaby et al. 1981; their Eq. 5.22), and T, P, and relative

320   humidity (RH) measurements from the AF (Table 3~~2~~), were used. Concentrations of oxygen and

321   water vapor and the oxygen and vapor path lengths are provided in Table 4~~3~~. The latter is the

322   vertical distance between the HP and the WKA. It was assumed that concentrations were

323   uniform over this path length.

324   Attenuation by cloud water was derived using the WKA-measured T (Table 3~~2~~), the

325   WKA-measured LWC, path length (Table 4~~3~~), and an attenuation formula (Liebe et al. 1989;

326   Vali and Haimov 2001). The LWC applied in the formula is the maximum of CDP

327   measurements acquired between t_0 - 10 s and t_0. This interval coincides with the interval the

328   WCR's down-looking antenna was used to acquire reflectivities over the HP (Sect. 3.5). The

329   path length for cloud water was derived as the vertical distance between cloud base [derived

330   thermodynamically using AF measurements (Table 3~~2~~)] and flight level. LWC was assumed

331   uniform, at the maximum value, over the path length.

332   Snow particle mass concentration is typically reported as an ice water content (IWC, g m^{-3}

333   ^{3}) (Liu and Illingworth 2000). The contribution of IWC to attenuation was calculated using

334 measurements in Nemarich et. al (1988), who reported an attenuation coefficient equal to 0.9

335 dB/km per unit of IWC. Also used were retrievals of IWC acquired using the down-pointing

336 WCR antenna. There are several steps in the calculation. First, all profiles of dBZ acquired

337 between t_0 - 10 s and t_0 were selected. Second, a maximum dBZ was selected at each of the

338 down-beam range gates (Table 21). Third, the dBZ maxima were increased by the overall two-

339 way attenuation in the final column of Table 43. Fourth, the profile of attenuation-corrected dBZ

340 was converted to a profile of attenuation-corrected Z. Fifth, a Z-to-IWC parameterization was

341 applied (IWC = $0.10 \cdot Z^{0.51}$; PV11; their Table 3). Sixth, the IWC profile was integrated, and the

342 derived ice water path was divided by the snow particle path length (Table 43). This calculation

343 produced a time- and range-averaged maximum IWC (Table 43). This IWC is the value applied

344 in the attenuation calculation.

345   Two-way attenuations (ΔdB), summed over contributions from the four components, are

346 presented in the final column of Table 43. Attenuation by snow and attenuation by liquid were

347 the most important components (> 50 %) on December 15 and January 3, respectively. Vapor

348 contributed 32 % to the overall on December 15, and the combination of vapor and snow

349 contributed 45 % on January 3. Equation 1 shows how an attenuation-corrected reflectivity (Z')

350 was derived using an uncorrected reflectivity (Z) and the ΔdB .

351

352      $$Z' = 10^{\left[\left[10 \cdot \log_{10}(Z) + \Delta dB\right]/10\right]}$$ (1)

353   Table 32 – Atmospheric state averages

354

Date	WKA [a] Track Altitude, m	WKA [a] T, °C	AF [b] T, °C	AF [b] RH, %	WKA [a, c] Track Vector	WKA [a, c] Wind Vector	AF [b, c] Wind Vector
14/15 December 2016	4546	-13.9	-6.3	86	310 / 130	274 / 32	250 / 8.5
3 January 2017	4196	-21.7	-14.6	77	280 / 120	265 / 27	260 / 5.4

355
356

357   [a] Altitude, temperature, track vector, and horizontal wind vector data obtained by averaging 1 Hz

358   WKA measurements. The averaging interval is 60 s and the interval starts at the overflight time,

359   minus 60 s, and ends at the overflight time.

360

361   [b] Temperature (T), relative humidity (RH), and horizontal wind vector data from sensors on the

362   US-GLE AmeriFlux tower (Sect. 2.1). The wind sensor was deployed at 26 m AGL (3223 m

363   MSL) and the T/RH sensor was deployed at 23 m AGL (3220 m MSL). The AF measurements

364   correspond to 30-minute averages closest to the overpass time. In the AF data set, time stamps on

365   the relevant AF recordings are 00:00 UTC (15 December 2016) and 20:30 UTC (3 January

366   2017).

367

368   [c] Vectors are presented in the following format: Direction of motion (degree relative to true

369   north) / speed (m s^{-1}).

370   Table 4~~3~~ – Attenuating component concentration, one-way pathlength, and the overall two-way attenuation

Date	Conc. Oxygen, kg m^{-3}	Conc. Vapor, kg m^{-3}	Maximum LWC, g m^{-3}	Maximum IWC, g m^{-3}	One-way Pathlength [a] Oxygen, Vapor, and Snow, km	One-way Pathlength [b] Cloud Water, km	Overall Two-way Attenuation, ΔdB
15 December 2016	0.21	2.7x10^{-3}	0.01	0.27	1.54	1.09	1.41 [c]
3 January 2017	0.21	1.3x10^{-3}	0.08	0.09	1.19	0.59	1.01 [d]

371

372   [a] Vertical distance between HP and WKA

373

374   [b] Vertical distance between cloud base [derived thermodynamically using AF measurements (Table 3~~2~~)] and WKA

375

376   [c] One-way attenuation coefficients are 0.03 dB/km for oxygen (Ulaby et al. 1981), 0.14 dB/km for vapor (Ulaby et al. 1981), 0.056

377   dB/km for cloud water (Liebe et al. 1989; Vali and Haimov 2001), and 0.24 dB/km for snow particles (Nemarich et. al 1988).

378

379   [d] One-way attenuation coefficients are 0.03 dB/km for oxygen (Ulaby et al. 1981), 0.073 dB/km for vapor (Ulaby et al. 1981), 0.49

380   dB/km for cloud water (Liebe et al. 1989; Vali and Haimov 2001), and 0.077 dB/km for snow particles (Nemarich et. al 1988).

381

382 **3.3 - Correction of Doppler Velocity**

383   We accounted for bias in V_D (Sect. 2.3) due to deviation of the down-looking WCR

384 antenna from vertical. This was done by applying the correction described in Zaremba et al.

385 (2022) (their Eq. A4). The west-to-east and south-to-north particle velocities used in the

386 correction were assumed to be equal to component wind velocities. The latter were expressed as

387 linear functions of altitude using the information in the penultimate and last columns of Table 3~~2~~.

388 The component velocities as functions of altitude and the linear equations relating velocity and

389 altitude are provided in the Appendix.

390 **3.4 - Hotplate Measurement of Wind Speed**

391   Here we compare the hotplate-derived wind speed to wind speed derived using an

392 R.M.Young rotating anemometer (R.M.Young 2001). The second of these is symbolized U_{RMY}

393 and the basis for the first (U_{PRO}) is a proprietary algorithm (Sect. 2.4). We are doing this

394 comparison because B14 showed that U_{PRO} can be high-biased, relative to a conventional

395 anemometer, and because U_{PRO} is the primary determinant of the rate that the up-viewing plate

396 dissipates sensible heat energy. Diagnosis of that heat transfer rate is our basis for calculating the

397 liquid-equivalent snowfall rate (Z18). The U_{PRO} also determines the snow particle catch

398 efficiency and the latter was used in calculations of the undercatch-corrected liquid-equivalent

399 snowfall rate (Sect. 2.4).

400   The comparisons reported here were done at the Laramie, WY Airport in December

401 2019, and in January 2020. Compared to the HP site, the Laramie Airport site (indicated LA in

402 Fig. 1) is free of obstruction, out to 120 m, and experiences larger wind speeds. By mounting the

403 hotplate and the R.M.Young anemometer on rigid metal pipes, the hotplate's heated horizontal

404   surfaces (the up- and down-viewing plates seen in Fig. 1 of Z18) and the anemometer's spinning

405   axis (oriented horizontally) were both positioned at 2 m AGL. The pipes were separated

406   horizontally by 5 m. There was no precipitation on the days selected for the wind speed

407   comparisons. The values of U_{PRO} and U_{RMY} we analyzed were recorded with a data system that

408   time stamped the 1 Hz U_{PRO} and 1 Hz U_{RMY} with a relative timing accuracy no worse than 1 s.

409   A wind speed comparison - from 13 December 2019 - is shown in Fig. 4a. U_{PRO} was

410   brought into the comparison by sampling it once per minute from files containing 1 Hz

411   recordings of the one-minute running-average U_{PRO} (Sect. 2.4). U_{RMY} was brought into the

412   comparison by starting with files containing 1 Hz recordings and converting these to one-minute

413   averages. Fig. 4a shows no evidence of bias and Fig. 4b demonstrates that the average absolute

414   departure between the U_{PRO} and U_{RMY} (both one-minute averages) is no larger than 1~~0.5~~ m s^{-1}.

415   Table 5~~4~~ has eight more precipitation-free comparisons. Included in the table are temperature

416   and wind speed averaged over the comparison intervals (4 to 20 UTC), the slope of the linear-

417   least-squares fit line (forced through the origin, red line), and the lower and upper quartiles of the

418   slope. The quartiles were calculated using the method of Wolfe and Snider (2012). In contrast to

419   Figs. 4a-b, Figs. 4c-d make the comparison using 1 Hz values of U_{PRO} and U_{RMY}. The larger

420   scatter and larger average absolute departure seen in these panels is a consequence of the

421   hotplate's limited time response, compared to the R.M.Young. We quantify the hotplate's

422   response time in terms of a calculated thermal response time. During wintertime at the Laramie

423   Airport, and with wind speed at 5 m s^{-1}, the down-viewing plate's thermal response time is

424   approximately 60 s (results not shown). Because the temperature of the down-viewing plate is

425   actively controlled, this does not translate to a 60 s lag between changes in wind speed and the

426   hotplate response. The U_{PRO}/U_{RMY} departure is most evident at $U_{PRO} > 5$ m s^{-1} (Fig. 4d) but this is

427   not a concern for U_{PRO} on 14/15 December 2016 or on 3 January 2017. Snider (2023)

428   demonstrated that the U_{PRO} was less than 5 m s^{-1} at the hotplate during the two WKA overflights.

429

430

431

432

433

434

435

436

437

438

439

440

441

442

443
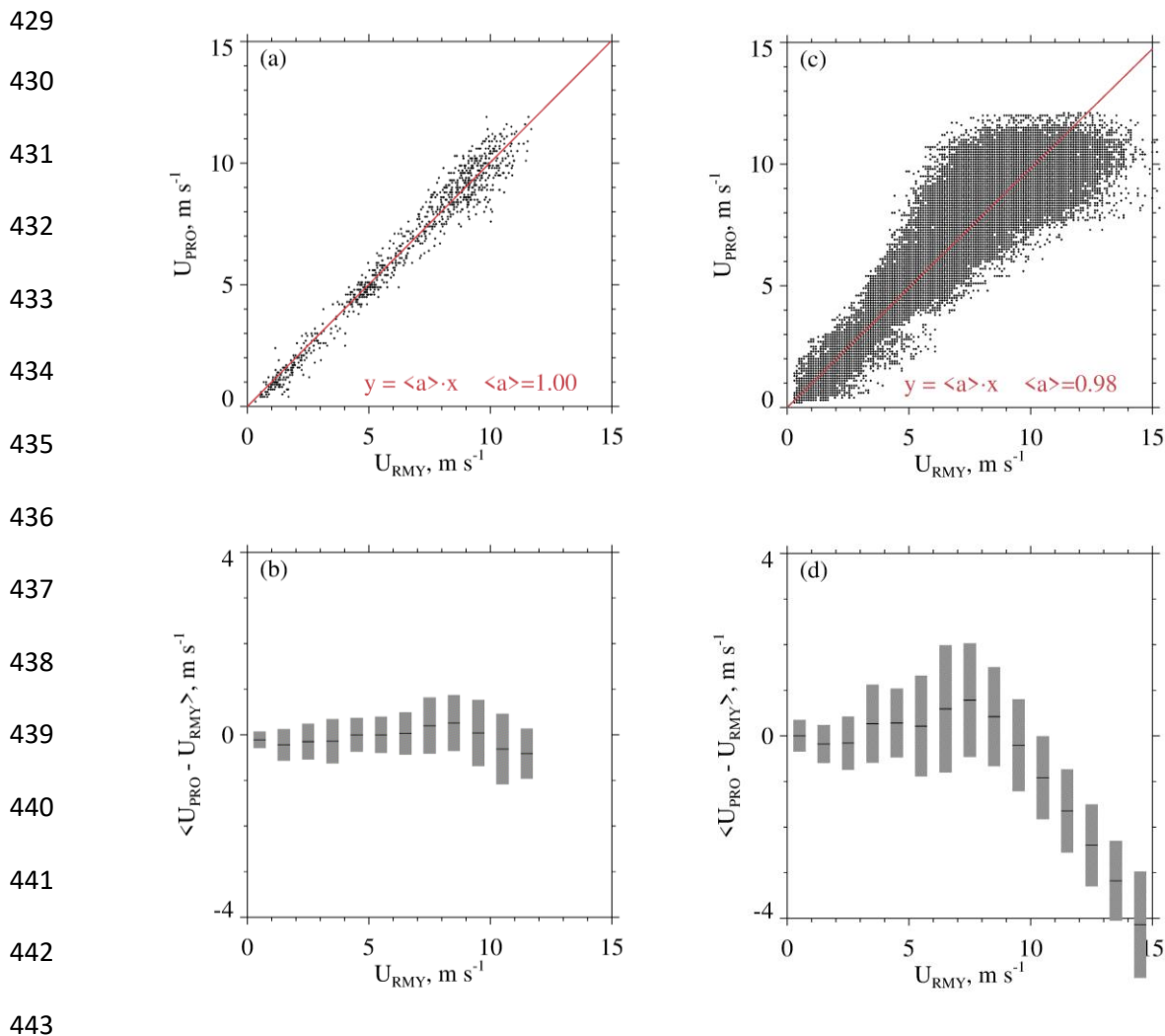
444   Figure 4 – (a) Scatterplot of one-minute-averaged U_{PRO} and one-minute-averaged U_{RMY}.

445   Measurements were acquired at the Laramie, WY Airport 13 December 2019. The red line is a

446   linear-least-squares fit line (forced through the origin). (b) Average departure between one-

447   minute-averaged U_{PRO} and one-minute-averaged U_{RMY}. Average departures were calculated for

448   discrete U_{RMY} intervals, and the averages are indicated with short black horizontal lines. Gray

449   bars indicate ± 1 standard deviation. (c) Same as in (a) except for 1 Hz values of U_{PRO} and U_{RMY}.

450   (d) Same as in (b) except for 1 Hz values of U_{PRO} and U_{RMY}.

451

452

453   Table 54 - U$_{PRO}$ versus U$_{RMY}$ correlations

454

Date, UTC [1]	$\langle T \rangle$ [2], °C	$\langle U \rangle$ [2], m s^{-1}	$\langle a \rangle$ [3]	a [4] First Quartile	a [4] Third Quartile
7 December 2019	-0.40	5.40	1.00	0.90	1.04
8 December 2019	2.70	4.10	0.99	0.90	1.04
10 December 2019	-5.20	3.80	0.99	0.83	1.04
13 December 2019	-1.50	6.60	1.00	0.93	1.06
18 December 2019	-6.20	3.60	0.99	0.92	1.04
19 December 2019	-6.90	2.70	0.95	0.84	0.99
6 January 2020	-6.40	8.80	1.01	0.96	1.06
8 January 2020	0.30	4.20	1.00	0.87	1.05
11 January 2020	-7.20	7.00	1.02	0.97	1.08

455

456

457   [1] Statistics presented are based on one-minute-averaged U$_{PRO}$ and one-minute-averaged U$_{RMY}$

458   measurements made between 04:00 to 20:00 UTC.

459

460   [2] Interval-averaged temperature and interval-averaged wind speed.

461

462   [3] Slope of the one-minute-averaged U$_{PRO}$ versus one-minute-averaged U$_{RMY}$ linear-least-squares

463   fit line, forced through the origin.

464

465   [4] Quartiles of the slope (see text)

466

467   **3.5 – Combined Aircraft and Surface Measurements**

468   Figure 5 has WCR and WKA measurements starting 100 s prior to t_0 and ending at t_0.

469   The sequences in Figs. 5a and 5c are reflectivities from both the up- and down-looking antennas.

470   In Fig. 5a the flight track (black dashed horizontal line) is at 4550 m and in Fig. 5c the flight

471   track is at 4200 m. At the t_0 in Fig. 5a, below the WKA, the maximum radar echo is +6 dBZ (Z =

472   4 mm^6 m^{-3}) and in Fig. 5c the maximum is -3 dBZ (Z = 0.5 mm^6 m^{-3}). Supercooled liquid water

473   was detected as the aircraft approached the ridgeline (Fig. 5b) and during the last 10 seconds of

474   the time sequence in Fig. 5d. During these encounters with supercooled liquid, the maximum

475   LWC values were 0.03x10^{-3} and 0.08x10^{-3} kg m^{-3} on 14 December 2016 and 3 January 2017,

476   respectively. Values of N (Sect. 2.2) at times of maximal LWC were 3x10^6 and 100x10^6 m^{-3} on

477   14 December 2016 and 3 January 2017, respectively. Even on 3 January 2017, the <D> (Sect.

478   2.2) associated with maximum LWC was sufficient for hexagonal plate crystals with diameter

479   larger than 100 μm to collide with the observed droplets with efficiencies > 0.1 (Wang and Ji

480   2000).

481   We temporally and spatially averaged the values of Z we compared with time-averaged

482   values of S. There are two reasons for this: 1) As discussed in Sect. 3.1, the WCR did not sample

483   Z exactly over the hotplate, and furthermore, the width of radar beam at 1500 m range - roughly

484   the distance between the aircraft and the ground at the overflight times - is 30 m and thus

485   considerably smaller than the minimum horizontal distance between the aircraft and the HP. 2)

486   Compared to the WCR, the hotplate is a relatively slow-response measurement system whose

487   output is commonly averaged over one-minute intervals (Z18).

488

489 FIGURE 5 WAS REVISED IN REVISION3.

490

491

492

493

494

495

496
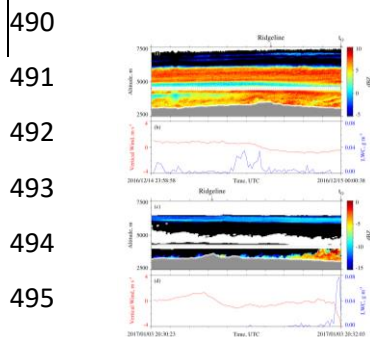
497

498

499

500

501

502

503

504

505

506

507

508

509

510

511

512

513 Figure 5   (a) 100 s of WCR reflectivity and (b) 100 s of LWC and gust probe vertical wind

514 velocity ending at t_0 on 14/15 December 2016. (c) 100 s of WCR reflectivity and (d) 100 s of

515 LWC and gust probe vertical wind velocity ending at t_0 on 3 January 2017. In (a) and (c), above

516 and below the flight track, is the roughly 200-m-deep WCR blind zone, reflectivity above

517 (below) the flight track is from the up-looking (down-looking) WCR antenna, black indicates

518 dBZ values smaller than minimum indicated in the color bar, white immediately above the

519 terrain indicates echo that was discarded because of ground clutter, and white above the ground

520 clutter and outside of the blind zone indicate dBZ < minimum detectable signal.
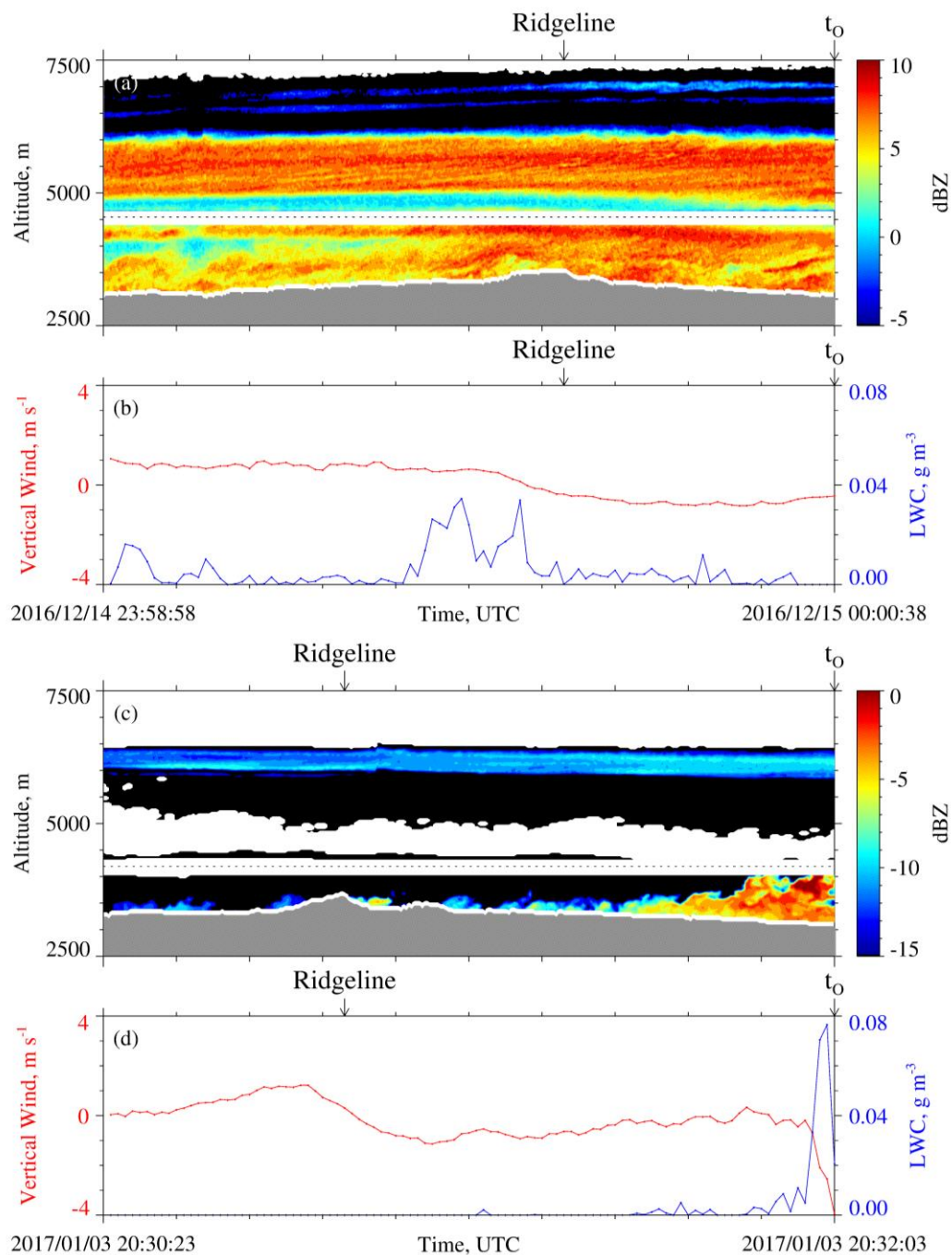
Figure 5 – (a) 100 s of WCR reflectivity and (b) 100 s of LWC and gust probe vertical

wind velocity ending at t_0 on 14/15 December 2016. (c) 100 s of WCR reflectivity and (d) 100 s

of LWC and gust probe vertical wind velocity ending at t_0 on 3 January 2017. In (a) and (c),

above and below the flight track, the roughly 200-m-deep WCR blind zone is evident,

reflectivity above (below) the flight track is from the up-looking (down-looking) WCR antenna,

540   black indicates dBZ values smaller than the minimum indicated in the color bar, white

541   immediately above the terrain indicates echo that was discarded because of ground clutter, and

542   white above the ground clutter and outside of the blind zone indicate dBZ < minimum detectable

543   signal.

544   In our analysis, t~~T~~he HP measurements were averaged over two adjacent 60 s intervals.

545   The first extends from t_0 to $t_0 + 60$ s (Fig. 6a) and the second from $t_0 + 60$ s to $t_0 + 120$ s (Fig.

546   6c). In Fig. 6a and in Fig. 6c, $t_{HP,B}$ symbolizes an interval's beginning time and $t_{HP,E}$ symbolizes

547   an interval's ending time. Formulas describing how these times were related to the beginning and

548   ending time of a corresponding WCR averaging interval are in the Appendix. Fig. 6b is a

549   schematic of the first WCR averaging interval and Fig. 6d is a schematic of the second. Again,

550   the subscripts "B" and "E" are used to indicate averaging beginning and ending times. Figures 6b

551   and 6d both have lines at the top of an averaging interval/domain. The slopes of these lines are

552   proportional to the ratio of two speeds. These speeds are a maximum likely snow particle speed

553   toward the ground (v_p) and a horizontal wind advection speed (v_w). The v_p was calculated

554   using averaged vertical-component Doppler velocities and v_w was calculated using a vertical

555   profile of horizontal winds, based on WKA horizontal wind measurements and AF horizontal

556   wind measurements (Figs. A1a-b), and using the WKA track vector (Table 3~~2~~). An altitude (z' ~~z~~

557   = 3400 m) was assumed in the calculation of v_w. This is the altitude of the ridges west and

558   northwest of the HP site (Figs. 3a-b). Picking the altitude to be either z' ~~z~~= 3200 m or z' ~~z~~=

559   3600 m does not alter our findings.

560

561
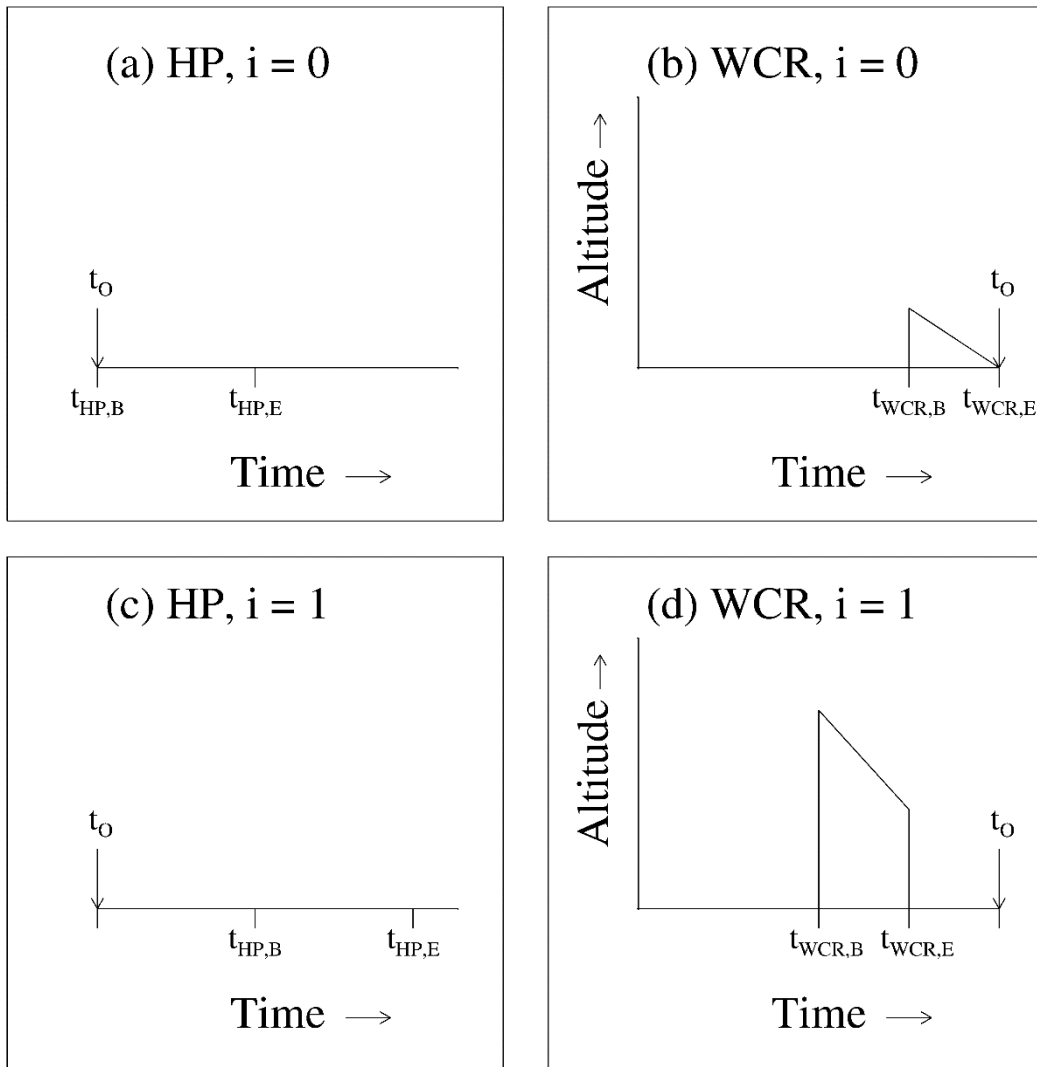
Figure 6 – (a and c) Representations of the $i = 0$ and $i = 1$ HP averaging intervals. (b and d)

Representations of the $i = 0$ and $i = 1$ WCR averaging intervals/domains. The t_0 is shown in all

panels. The subscripts "B" and "E" indicate beginning and ending times of the HP averaging

(panels a and c) and the beginning and ending times of the WCR averaging (panels b and d).

586

587   All panels in Fig. 6 are labeled with an index designating either the first averaging

588   interval $(i = 0)$ or the second averaging interval $(i = 1)$. Figures 7 and 8 present hotplate

589   snowfall measurements from 14/15 December 2016 and 3 January 2017. In these, and in

590   subsequent figures, colored circles surround the $i = 0$ and $i = 1$ indexes, blue is used to color-

591   code 15 December 2016, and red is used to color-code 3 January 2017. Additionally, Fig. 8 has

592   an $i = 2$ averaging interval. This is a special case discussed at the end of this section.

593   Figures 9a-b and Figs. 10a-b have enlarged views of the altitude-time WCR crossections

594   recorded on the two flight days. Different from Fig. 5a and Fig. 5c, these measurements are only

595   from the WCR's down-looking antenna. Additional differences are the following: 1) The plots

596   are set up so that Z and $\overline{V_D} V_D$ structures downwind of the hotplate can be seen. These structures

597   are discussed in the following section. 2) The WCR measurements are shown for 50 s of flight.

598   With the WKA ground speed approximately 125 m s^{-1} (Table 3~~2~~), the distance along the abscissa

599   is 6250 m. 3) Colored circles that surround the ~~$i = 0$~~ indexes are placed below the WCR

600   averaging intervals/domains. The latter are drawn with solid black lines and are seen to overlay

601   both the Z and $\overline{V_D} V_D$ altitude-time crossections. Consistent with Figs. 6b and 6d, and the

602   Appendix, one of these black lines is vertical and another~~the other~~ is negatively sloped. Figs.

603   10a-b also have the $i = 2$ ~~$i = 2$~~ intervals/domains discussed at the end of this section.

604

605

606

607   THIS FIGURE WAS REVISED IN REVISION3.

608

609

610

611
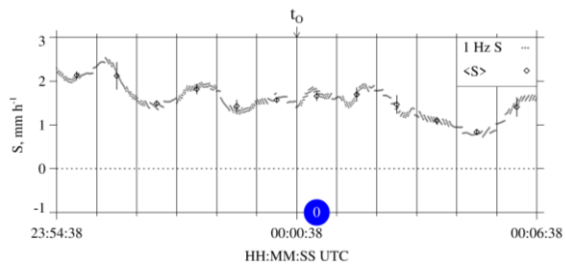
612

613

614

615

616

617
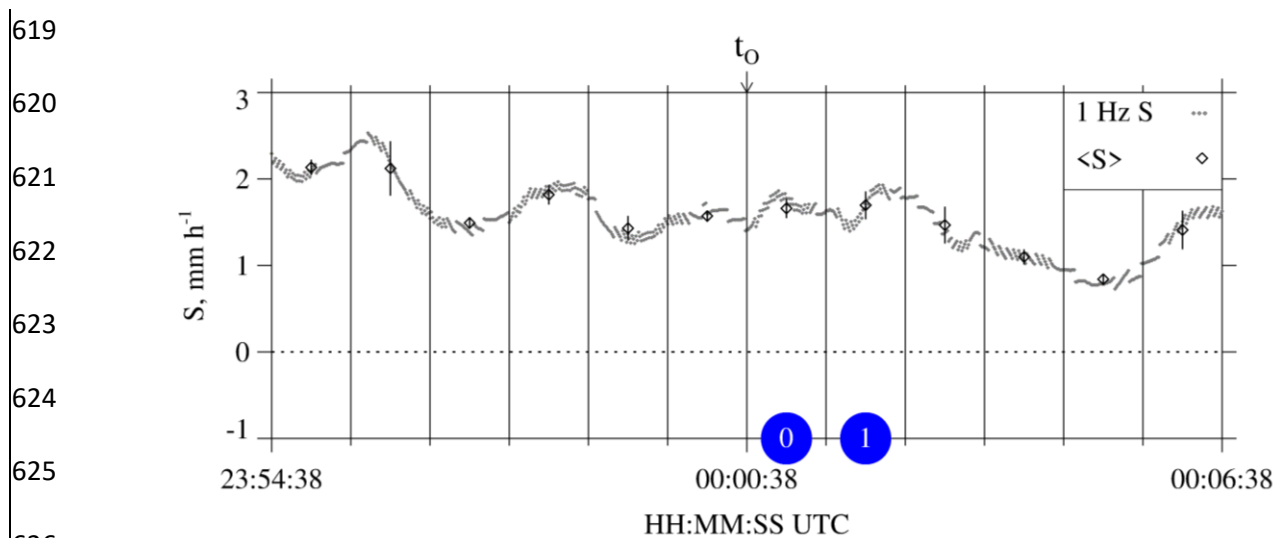
618

Figure 7 – Twelve minutes of HP snowfall measurements from 14/15 December 2016. Gray dots are S values calculated using hotplate output recorded at 1 Hz. Black diamonds are the one-minute-averaged values (± 1 standard deviation). The t_0 is shown above the panel and the blue circles designates the $i = 0$ and $i = 1$ HP averaging intervals.

633   THIS FIGURE WAS REVISED IN REVISION3.

634

635

636

637

638

639

640

641

642

643

644

645

646

647

648

649

650

651

652

653
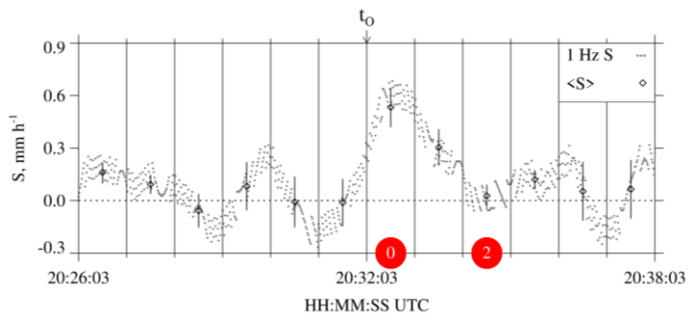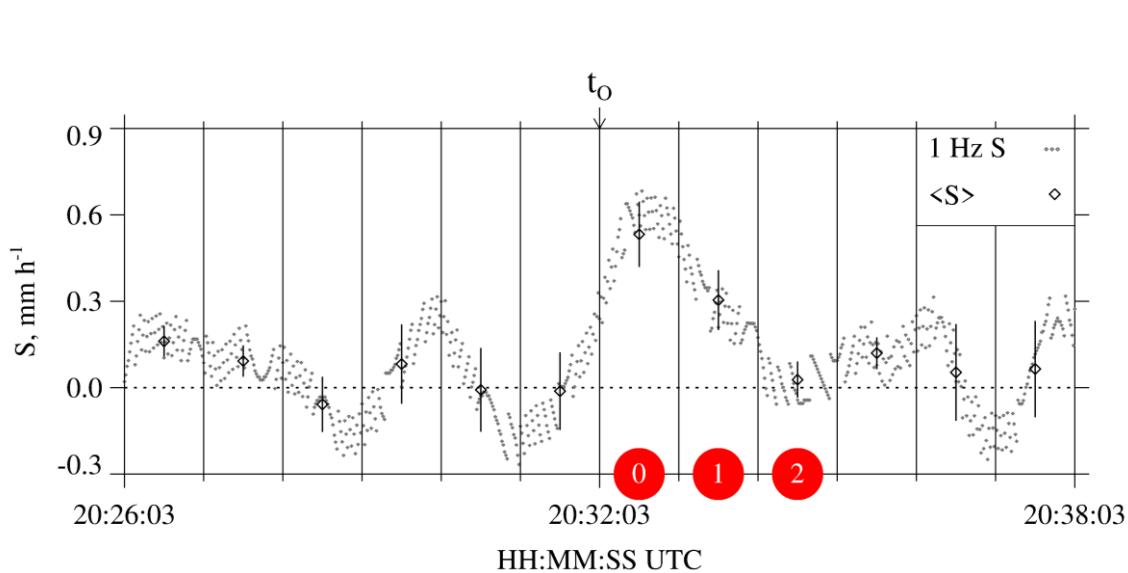
654 Figure 8 – Twelve minutes of HP snowfall measurements from 3 January 2017. Gray dots are S

655 values calculated using hotplate output recorded at 1 Hz. Black diamonds are the one-minute-

656 averaged values (± 1 standard deviation). The t_0 is shown above the panel and , a red circles

657 designates the $i = 0$, $i = 1$, and $i = 2$ HP averaging intervals, and a red circle designates the $i = 2$

658 HP averaging interval. The $i = 2$ intervallatter is a special case discussed at the end of Sect. 3.5.

659

660   THIS FIGURE WAS REVISED IN REVISION3.

661

662

663

664

665

666

667

677

678

679

680

681

682

683

684

685

686

687

688
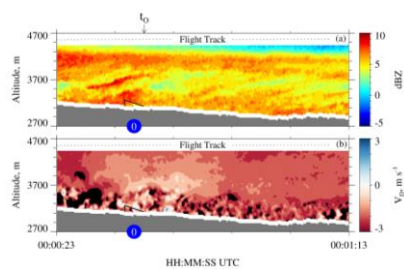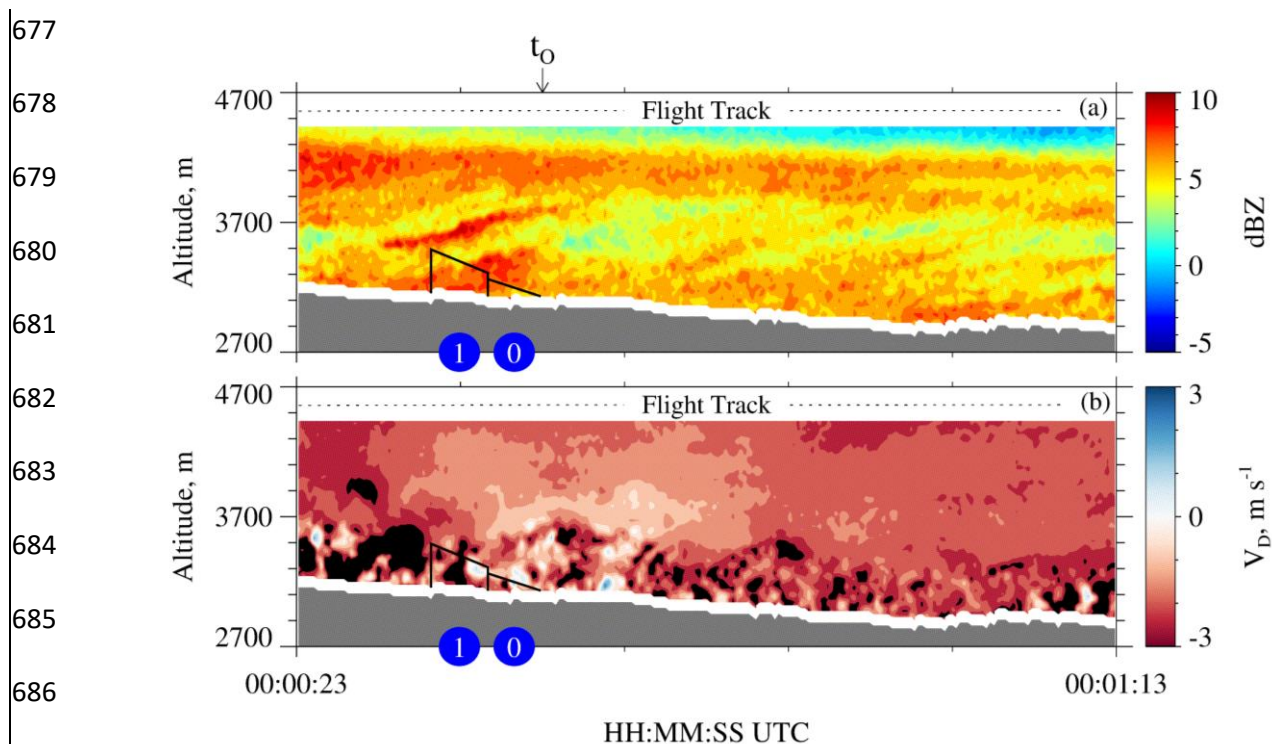
689   Figure 9 – 50 s of measurements from the down-looking WCR antenna on 15 December 2016.

690   (a) Crossection of reflectivity t_0 - 15 s to t_0 + 35 s. (b) Crossection of Doppler velocity t_0 - 15 s to

691   t_0 + 35 s. The t_0 is shown above the top panel. In both panels, the solid black lines (vertical and

692   sloped) encompass the $i = 0$ and $i = 1$ WCR averaging intervals/domains and blue circles

693   designate the the $i = 0$ WCR averaging intervals.

694

695   THIS FIGURE WAS REVISED IN REVISION3.

696

697

698

699

700

701

702

703

704

705

706

707

708

709

710
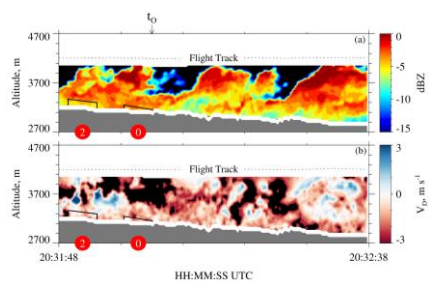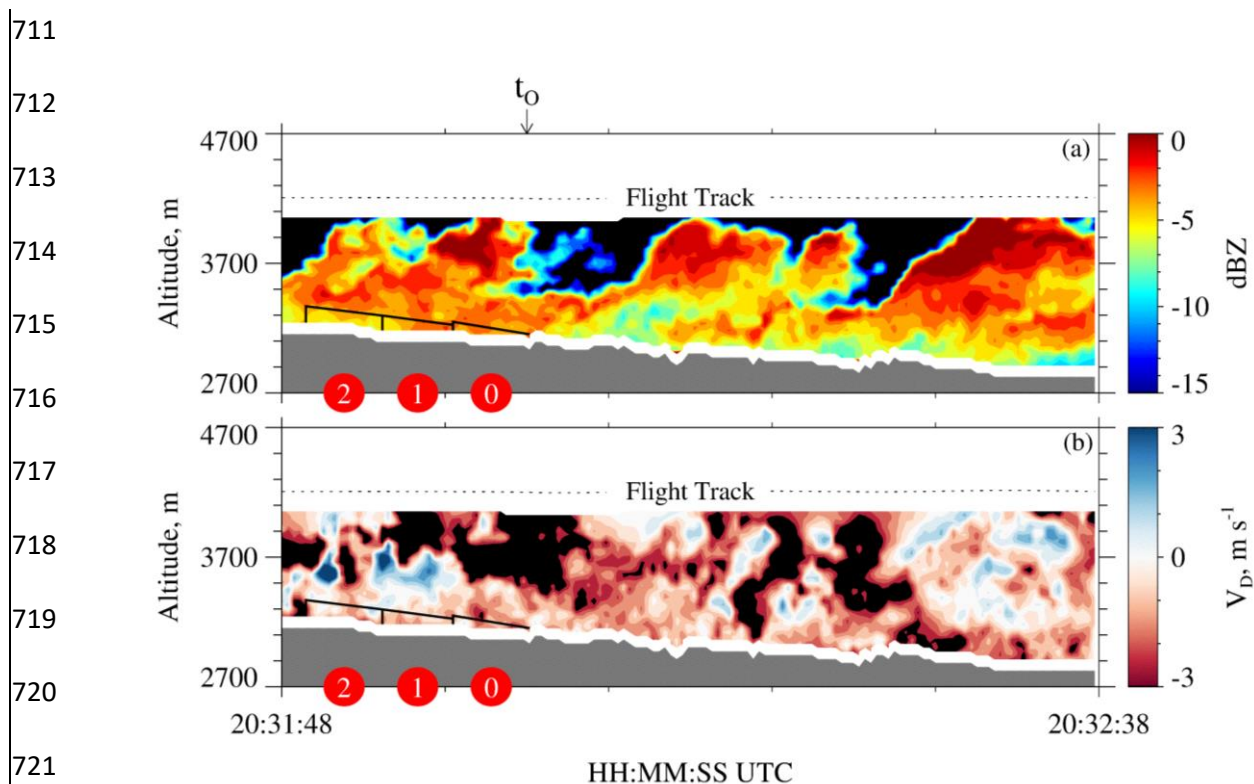
Figure 10 – 50 s of measurements from the down-looking WCR antenna on 3 January 2017. (a)

Crossection of reflectivity t_0 - 15 s to t_0 + 35 s. (b) Crossection of Doppler velocity t_0 - 15 s to t_0

+ 35 s. The t_0 is shown above the top panel. In both panels, the solid black lines (vertical and

sloped) encompass the $i = 0$, $i = 1$, and ~~and~~ $i = 2$ WCR averaging intervals/domains and~~, two~~ red

circles designate the $i = 0$, $i = 1$, and $i = 2$ ~~$i = 0$~~ WCR averaging intervals/domains~~averaging~~

~~interval.~~, ~~and two red circles designate the $i = 2$ WCR averaging interval.~~ The $i = 2$

interval/domain is ~~$i = 2$ intervals/domains are~~ a special case discussed at the end of Sect. 3.5.

732   The $i = 0$ and $i = 1$ averages of S and Z are presented in Table 65 and the corresponding

733   averaging intervals are viewable in Fig. 7 and Fig. 9a (15 December 2016) and in Fig. 8 and Fig.

734   10a (3 January 2017). The $i = 1$ averages are also presented in Table 5. According to the

735   averaging scheme (Fig. 6), the $i = 1$ HP averaging interval is time-shifted positively compared to

736   the $i = 0$ HP averaging interval and the $i = 1$ WCR averaging interval is time-shifted negatively

737   compared of the $i = 0$ WCR averaging interval. This arrangement of the averaging intervals is

738   one way to average while also accounting for wind advection of the snow particles.

739   As discussed earlier in this section, the averaging scheme initializes with 60-second

740   blocks of HP data between $t_o{}^{t_0}$ and $t_o{}^{t_0} + 120$ s. When we applied the scheme to data from 3

741   January 2017, but outside the specified time range, an inconsistency was documented. This is

742   apparent in Fig. 8, where the $t_o{}^{t_0} + 120$ s to $t_o{}^{t_0} + 180$ s interval (i.e., the $i = 2$ $i = 2$ interval) has

743   negligible average S, while in Fig. 10, the $i = 2$ $i = 2$ interval has a non-negligible average Z (~

744   0.3 mm^6 m^{-3}). A firm explanation is not available for the inconsistency, but a factor may be the

745   convective nature of the fields in Figs. 10a-b. Because of the inconsistency, only averages

746   corresponding to the $i = 0$ $i = 0$ and $i = 1$ $i = 1$ intervals arewere analyzed further.

747

748 Table 6 – Average wind measurements, average hotplate measurements, average WCR measurements, and attenuation-corrected

749 reflectivities

Date	v_w [a] $\mathrm{m\ s^{-1}}$	i index	$S_{HP} \pm \sigma$ [b], $\mathrm{mm\ h^{-1}}$	WCR Samples [c]	$\langle V_D \rangle$ [d], $\mathrm{m\ s^{-1}}$	σ_{V_D} [e] $\mathrm{m\ s^{-1}}$	v_p [f] $\mathrm{m\ s^{-1}}$	$\langle Z \rangle \pm \sigma_Z$ [g], $\mathrm{mm^6\ m^{-3}}$	Z' [h], $\mathrm{mm^6\ m^{-3}}$
15 December 2016	7.4	0	1.7±0.1	42	-1.3	0.9	2.2	4.9±2.1	6.8
15 December 2016	7.4	1	1.7±0.2	149	-1.8	1.2	3.0	5.6±1.1	7.8
3 January 2017	8.9	0	0.5±0.1	22	-0.9	0.8	1.7	0.49±0.05	0.62
3 January 2017	8.9	1	0.3±0.1	35	-0.8	0.4	1.2	0.50±0.10	0.63

750

751 [a] Horizontal wind advection speed (Eq. A7) calculated using values from the penultimate and last columns of Table 3.

752 [b] One-minute average of the undercatch-corrected liquid-equivalent snowfall rate (± 1 standard deviation). An example averaging

753 interval is the $i = 0$ interval in Fig. 7.

754 [c] Number of samples used to calculate the WCR statistics. The averaging intervals/domains (e.g., $i = 0$ in Figs. 9a-b and in Figs. 10a-

755 b) encompass the WCR samples which are the basis for the WCR statistics presented in this table.

756 [d] Average of Doppler velocity within the averaging intervals/domains.

757 [e] Standard deviation of Doppler velocity within the averaging intervals/domains.

758 [f] Maximum likely snow particle speed toward the ground (Eq. A8).

759 [g] Average reflectivity (± 1 standard deviation). These values are not corrected for attenuation.

760   [h] Attenuation-corrected reflectivities. These were derived using reflectivities from the penultimate column of this table, attenuations

761   from Table 4, and Eq. 1.

762

763

764 Table 5—Averaged wind, hotplate, and WCR measurements

Date	v_w[a], m·s^{-1}	i index	$\langle S\rangle\pm\sigma_S$[b], mm·h^{-1}	WCR Samples[c]	$\langle V_D\rangle$[d], m·s^{-1}	σ_{V_D}[e], m·s^{-1}	v_p[f], m·s^{-1}	$\langle Z\rangle\pm\sigma_Z$[g], mm^6·m^{-3}
15 December 2016	7.4	0	1.7±0.1	42	-1.3	0.9	2.2	4.9±2.1
15 December 2016	7.4	1	1.7±0.2	149	-1.8	1.2	3.0	5.6±1.1
3 January 2017	8.9	0	0.5±0.1	22	-0.9	0.8	1.7	0.49±0.05
3 January 2017	8.9	1	0.3±0.1	35	-0.8	0.4	1.2	0.50±0.10

765

766 [a] Horizontal wind advection speed (Eq. A7) calculated using values from the penultimate and last

767 columns of Table 2.

768

769 [b] One-minute average of the undercatch-corrected liquid-equivalent snowfall rate (± 1 standard

770 deviation). An example averaging interval is the interval in Fig. 7.

771

772 [c] Number of samples used to calculate WCR statistics in the penultimate four columns. The

773 averaging intervals/domains (e.g., $i=0$ in Figs. 9a-b and in Figs. 10a-b) encompass the averaged

774 WCR samples.

775

776 [d] Average of Doppler velocity within the averaging intervals/domains.

777

778 [e] Standard deviation of Doppler velocity within the averaging intervals/domains.

779

780 [f] Maximum likely snow particle speed toward the ground (Eq. A8).

781

782 [g] Average reflectivity (± 1 standard deviation). These values are not corrected for attenuation.

783

3.6 - Snow Particle Imagery

784

785   In Fig. 9a and Fig. 10a, the time for a snow particle to move the abscissa and ordinate

786   distances is different. The ratio of these two times is 2.6. This follows from our choice of

787   abscissa and ordinate ranges, from values of particle fall speed (1 m s^{-1}) and horizontal wind

788   advection speed (8 m s^{-1}), which we assumed, and from the WKA ground speed ($gs \sim 125$ m s^{-1};

789   Table 32). The assumed values are approximately consistent with values of $<V_D>$ and v_w , in

790   Table 65, and with the V_D sign convention (Sect. 2.3). We also used $gs = 125$ m s^{-1} to scale

791   (virtually) the time axes in Fig. 9a and Fig. 10a to a horizontal distance. Within the scaled

792   coordinate frames, we assumed that all snow particle trajectories have negative slope ($\Delta z / \Delta x = $ -

793   1 m s^{-1} / 8 m s^{-1} = -0.12) and that all trajectories are stationary. However, both assumptions seem

794   inconsistent with the reflectivity structures in Fig. 5a, where positively-sloped particle fall

795   streaks are evident at ~ 5500 m, inconsistent with Fig. 9a where positively-sloped fall streaks are

796   at ~ 3500 m, and inconsistent with the positively-sloped fall streaks in Fig. 10a. On both flight

797   days, the fall streaks evince particle sources that move horizontally and with a horizontal speed

798   that is larger than the $v_w = 8$ m s^{-1} applied in the estimate of the trajectory slope. It may be that

799   the source's horizontal speed is comparable to the flight-level WKA-derived horizontal wind (27

800   to 32 m s^{-1}; Table 32) but we do not have data needed to verify that assertion. Based on the

801   assumption that snow particles followed the fall streaks while both were advecting horizontally,

802   we looked *downwind* of the hotplate - at a time later than t_0 in Fig. 9a and Fig. 10a - for particles

803   that became those that produced snowfall at the hotplate.

804   Particle images from 15 December 2016 were analyzed using the 2DP. With this

805   instrument the maximum all-in particle size (in the horizontal direction perpendicular to flight) is

806   6400 µm and the particle size resolution is 200 µm (Sect. 2.2). Within the time interval picked

807   for this analysis (discussed below), particles sizing in the smaller of the two spectral modes, with

808   mode size ~ 400 µm, were more numerous (results not shown). Because the 400 µm particles are

809   poorly resolved by the 2DP, and the same can be said for somewhat larger particles, those

810   smaller than 1000 µm were excluded from the following analysis. Figure 11a shows imagery

811   from 12 s of measurements acquired near the end of the sequence in Fig. 9a (00:01:02 to

812   00:01:14). This time interval was selected by tracing forward from t_0, along the slope of the fall

813   streaks, to the flight level. Many of the particles are rounded (indicating riming) and a few have

814   arms likely due to incomplete conversion of branched crystals to rimed snow particles. The mode

815   size corresponding to these images is 1600 µm. No liquid water was detected with these particles

816   (LWC $< 0.01 \times 10^{-3}$ kg m^{-3}; Fuller 2020; her Fig. 8), but liquid was detected, at ~ 00:00:00, as the

817   aircraft approached the ridgeline (Figs. 5a-b).

818   Turning to imagery from 3 January 2017, the most appropriate location for analysis

819   would be through the second billow structure evident in Fig. 10a (i.e., very close to the middle of

820   the Fig. 10a sequence). This billow sourced a fall streak that terminated at the hotplate (i.e., at

821   the time t_0 indicated in the figure). However, the aircraft only clipped the top of this billow, and

822   it was only when sampling the billow seen ~ 13 s earlier that larger ice particle concentrations (~

823   20,000 m^{-3}) (Fuller 2020; her Fig. 10) and larger LWC (~ 0.08×10^{-3} kg m^{-3}; Fig. 5d) were

824   detected. Maximum reflectivities were the same in all three billows (Z ~ 1 mm^6 m^{-3}; 0 dBZ), so it

825   was assumed that imagery collected in the first billow (20:32:00 to 20:32:02) was representative

826   of what was falling toward the hotplate. The 2DS was used to image these particles (Fig. 11b);

827   with this instrument the maximum all-in particle size (in the horizontal direction perpendicular to

828   flight) is 1280 µm and the size resolution is 10 µm (Sect. 2.2). Most of the objects in Fig. 11b

829   appear to be rimed and their mode size is ~ 400 μm. It is also noted that particles smaller than

830   100 μm were eliminated from these images, however, compared to the ~ 400 μm particles those

831   smaller than 100 μm were significantly less abundant (results not shown).

832

833 (a)

834

835

836

837

838

839

840 (b)

841

842

843

844

845

846

847
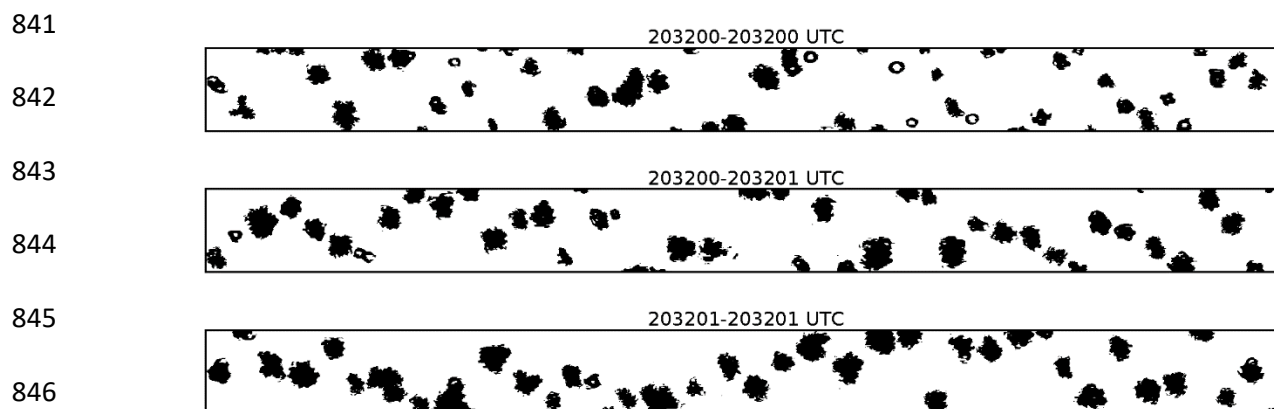
848 Figure 11 – (a) 2DP particle imagery from 15 December 2016. The height of the strips is 6400

849 µm. These particles are estimated to be representative of those that fell from flight level toward

850 the hotplate. (b) 2DS particle imagery from 3 January 2017. The height of the strips is 1280 µm.

851 These particles are estimated to be representative of those that fell from flight level toward the

852 hotplate.

853

854 **3.7 – S/Z Relationships**

855   Our S/Z pairs are presented in Table 6~~5~~ where the indexes ($i = 0$ and $i = 1$) are used to

856 indicate results derived for the averaging intervals. In the penultimate column of Table 6,

857 reflectivities are not corrected for attenuation, however, in the last column of Table 6 and in Fig.

858 12, the attenuation-corrected reflectivities are presented. ~~In Table 5, reflectivities are not~~

859 ~~corrected for attenuation, however, in Fig. 12a, attenuation-corrected reflectivities are plotted.~~

860 Reflectivities from the penultimate column of Table 6~~5~~, attenuations from Table 4~~3~~, and Eq. 1

861 were used to calculate the corrected reflectivities. Also shown in Fig. 12 (black filled circles) is a

862 subset of the S/Z pairs from PV11's Fig. 11 (0.01 < Z < 10 mm^6 mm^{-3}) and the PV11 best-fit line

863 (black). Results from PV11 are specified as S(ρ_1)/Z because those authors applied the lower of

864 two density-size functions (ρ_1), and the lower of two fall speed-size functions, with airborne

865 measurements, in calculations of snowfall rates (Sect. 1 and Table 1).

866   THIS FIGURE WAS REVISED IN REVISION3.

867

868

869

870
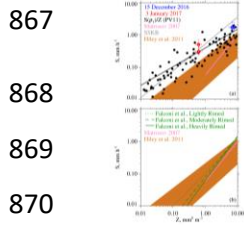
871

872

873

874

875

876

877

878

879

880

881

882

883

884   Figure 12 ~~a) Snowfall rate versus radar reflectivity. Colored circles indicate attenuation-~~

885   ~~corrected reflectivities (Table 3, Table 5, and Eq. 1) for the $i = 0$ and $i = 1$ averaging intervals.~~

886   ~~Error bars on these points represent the precision of the Z measurement (Sect. 2.3) and the~~

887   ~~precision of the S measurement (Sect. 2.4). The S(ρ_1)/Z points are a subset from PV11's Fig. 11~~

888   ~~(0.01 < Z < 10 mm^6·mm^{-3}). Also plotted is the PV11 best-fit line (black) (Sect. 1), the S/Z~~

889   ~~relationship from Matrosov (2007) (Sect. 1), the S/Z relationship abbreviated SSKB (Sect. 1),~~

890   ~~and the swath of S/Z relationships from Hiley et al. (2011) (Sect. 1). b) S/Z relationships from~~

891   ~~Falconi et al. (2018) (their Table 2) (Sect. 1), the Matrosov (2007) relationship, and the swath of~~

892   ~~S/Z relationships from Hiley et al. (2011) are shown.~~

893

894
895
896
897
898
899
900
901
902
903
904
905
906
907
908
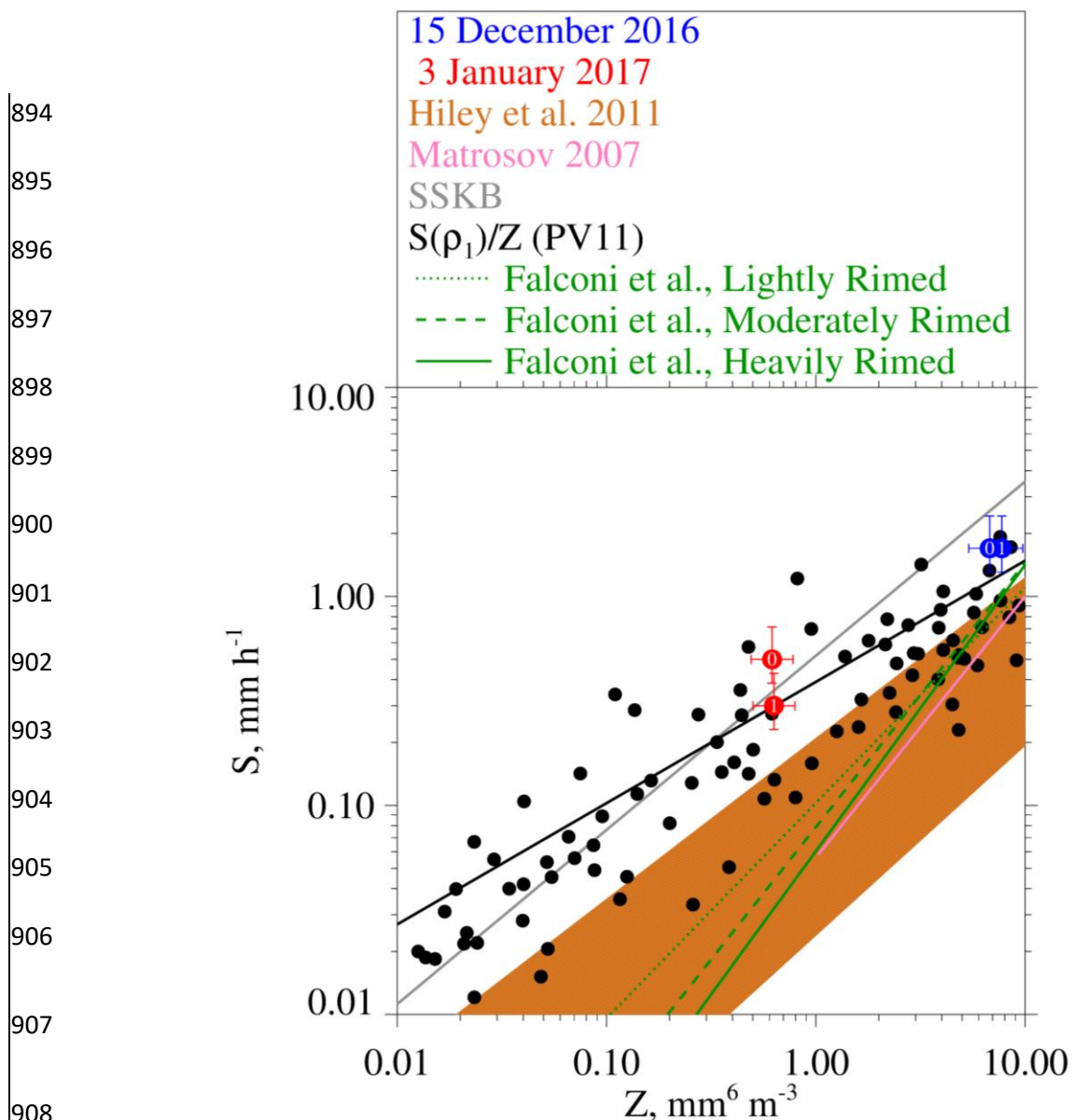
909   Figure 12 – Snowfall rate versus radar reflectivity. Red and blue circles are plotted at

910   attenuation-corrected reflectivities (Table 6) for the $i = 0$ and $i = 1$ averaging intervals. Error

911   bars on these points represent precisions of the reflectivity (Sect. 2.3) and snowfall rate (Sect.

912   2.4) measurements. Also plotted are the S/Z relationship lines from Sect. 1 and Table 1. These

913   are the S/Z lines defining the swath of S/Z relationships from Hiley et al. (2011), the S/Z

914   relationship from Matrosov (2007), the S/Z relationship abbreviated SSKB, PV11's best-fit line,

915   and the S/Z relationships from Falconi et al. (2018) (their Table 2). The $S(\rho_1)/Z$ points (black

916   filled circles) are a subset from PV11's Fig. 11 ($0.01 < Z < 10$ mm^6 mm^{-3}).

917   There are two potential biases in the values of snowfall rateS we tabulate measured

918   (Table 65) and plot (Fig. 12a). First, the two snowfall events had flight-level vertical wind

919   velocities (Figs. 5b and 5d) that were positive (upward) upwind of the ridgelinesummit, and vice

920   versa downwind of the ridgelinesummit. Except for the strongest downdraft on 3 January 2017,

921   the magnitude of this variance is ~ 1 m s^{-1} (Figs. 5b and 5d). Assuming 1 m s^{-1} was the

922   downward wind immediately over the hotplate, the snow particles would have approached the

923   HP gauge faster than their fall speed. Our basis for stating this is fall speeds for the mode sizes

924   discussed in Sect. 3.6 (1600 and 400 μm) and our assumption that the particles were graupel.

925   (Table 76 has these characteristic sizes and fall speeds.) However, the conjectured downdraft

926   speed is likely an overestimate - because of divergence occurring as the draft approached the

927   surface - and because the sizes in Table 76 likely underestimate what fell to the hotplate.

928   Relevant to the last of these assertions, we used the altitude/T/RH measurements (Table 32) to

929   calculate the vertical distance available for growth via riming, and thus for a fall speed increase,

930   between the flight level and the lifted condensation level. Assuming an adiabatically-stratified

931   liquid cloud and unit collection efficiency (these assumptions overestimate growth by riming),

932   and no change of particle crossection (underestimates growth by riming), our calculations

933   indicate that relative increases of size and fall speed were 40 and 20 %, respectively, on 3

934   January 2017, and that these relative increases were a factor-of-two larger on 15 December 2016.

935

936   Table 76 – Estimates of snow particle fall speed

Date	Mode Size, μm	Assumed Particle Type	Fall Speed, m s^{-1}	Reference
15 December 20165	1600	graupel	1.4	PV11; assuming ρ_1 in their Fig. 5
3 January 20176	400	graupel	0.7	PV11; assuming ρ_1 in their Fig. 5

937
938

939   Second, there is concern that values of S from 3 January 2017 are underestimated.

940   Although values of S must be > 0, we presented 1 Hz values (gray points, Fig. 8) approaching -

941   0.3 mm h^{-1}. Negative values resulted because we did not impose a threshold of 0 mm h^{-1} on the

942   uncorrected snowfall rates (this thresholding is discussed in Z18) and because negative snowfall

943   rate values (uncorrected for catch inefficiency) are amplified by the gauge-catch correction (Sect.

944   2.4). The implication is that 0.2 mm h^{-1} could be added to the one-minute averaged values of

945   snowfall rateS in Table 65 and in Fig. 12a. Here, the assumption is that an averaged S of -0.2

946   mm h^{-1}, in Fig. 8, is indicatingindicates no snowfall at the hotplate; however, because the

947   hotplate was operated autonomously (Sect. 2.1) we have no way to verify the assumption.

948

949 **4 – Results**

950 Figure 12~~a~~ shows our~~the~~ four snowfall rate/reflectivity~~S/Z~~ pairs (red and blue circles~~, our~~

951 ~~measurements~~) after the reflectivities were corrected for attenuation. The error bars on these data

952 pairs represent the precision of the Z measurement (Sect. 2.3) and the precision of the S

953 measurement (Sect. 2.4). Presentation clarity was what guided the selection of S and Z axis

954 ranges in this figure but with the consequence that 32 of PV11's S/Z pairs are not shown because

955 they plot at $Z > 10$ mm^6 m^{-3}. The way that the PV11 data pairs scatter closest to $Z = 10$ mm^6 m^{-3},

956 combined with the fact that the PV11 data pairs~~points~~ at $Z > 10$ mm^6 m^{-3} are not shown, could

957 lead to the interpretation that the slope describing the best-fit relationship, at Z approximately > 2

958 mm^6 m^{-3}, ~~-~~should be decreased relative to the actual slope of the PV11 best-fit line. Readers who

959 view PV11's Fig. 11 will conclude that this interpretation is not warranted. ~~The four S/Z pairs~~

960 ~~(red and blue circles) plot above the PV11 best-fit line but within the variability of PV11's S/Z~~

961 ~~pairs.~~

962 As is discussed in Sect. 1, c~~C~~omputation-based~~nal~~ W-band S/Z relationship have inputs

963 from parameterized descriptions of density, shape, fall speed, PSD, and particle size ~~(Sect. 1)~~.

964 The computation-based S/Z relationships are in the top three rows of Table 1; the subsequent two

965 rows of Table 1 have S/Z relationships that resulted from a hybridization of measurements and

966 calculations (PV11 and Falconi et al. 2018).~~Matrosov (2007) did calculations for the snow~~

967 ~~particle type known as aggregates. Hiley et al. (2011) did calculations for 20 snow particle types.~~

968 ~~Except for a S/Z calculation done for aggregate snowflakes, the calculations of Hiley et al.~~

969 ~~(2011) were for the particle type known as vapor-grown crystals. Hiley et al. (2011) did not~~

970 ~~model spherical snow particles. The latter were modeled by Surussavadee and Staelin (2007) and~~

971 ~~Kulie and Bennartz (2009). In Fig. 12a, the abbreviation SSKB is used to symbolize the~~

972 ~~computational S/Z relationship for spherical snow particles.~~

973   We now compare our snowfall rates (fourth column of Table 6) to snowfall rates where

974 they plot on an S/Z relationship line evaluated at one of our attenuation-corrected reflectivities.

975 The departure between these is reported as a relative S difference expressed as $|(S_{HP}-S)|/S$ where

976 S_{HP} is from Table 6 and where S is on an S/Z relationship line. All possible comparisons are

977 presented graphically in Fig. 12. Table 1 has both the minimum relative S differences and the

978 salient maximum relative S differences. The comparisons will be discussed in the order of

979 presentation in Table 1.

980   In comparisons of our snowfall rates and the upper-limit S/Z relationship line from Hiley

981 et al. (2011) the relative difference is no smaller than 0.7 and 1.0 on 15 December and 3 January,

982 respectively. These minimum relative differences exceed the hotplate precision (Sect. 2.4) by at

983 least a factor of two. It is concluded that our paired values of undercatch-corrected precipitation

984 rate and attenuation-corrected radar reflectivity provide evidence that a calculation of S based on

985 the Hiley et al. (2011) upper-limit, when applied to rimed snow particles, is associated with a

986 low-biased estimate of S. A retrieval based on Hiley et al.'s average S/Z relationship (not

987 shown), which bisects the orange region in Fig. 12, corresponds to an even larger low bias. This

988 is a concern because Hiley et al. (2011) used their average S/Z relationship to retrieve global

989 snowfall distributions and since global observations reported in Wang et al. (2013) document the

990 frequent occurrence of supercooled liquid within snowing clouds.

991

992   Fig~~ure~~. 12~~a~~ shows the separation between our measurements ~~S/Z pairs~~ and the Matrosov

993   (2007) calculation. The separation is about a factor of two (minimum relative difference = 1.4)

994   for the points obtained on 15 December 2016 and corresponds to an underestimation of S (low

995   bias) when compared to our measurements. The points from~~obtained on~~ 3 January 2017 plot at

996   an attenuation-corrected reflectivity ~~Z~~ smaller than the lower-limit of the calculation (Matrosov

997   2007). Since the particle images (Fig. 11a-b) reveal no evidence of~~for~~ the particle type modeled

998   by Matrosov (2007) (aggregate ~~snowflake~~s), it is not surprising that the Matrosov S/Z

999   relationship~~calculation~~ is not representative of our measurements.

1000   ~~Departures between our S measurements (Fig. 12a) and S/Z calculations from Hiley et al.~~

1001   ~~(2011) were evaluated as the vertical distance between the top of the orange region and our S/Z~~

1002   ~~data pairs. Snowfall rates at the top of the orange region were calculated using attenuation-~~

1003   ~~corrected reflectivities (Eq. 1 and Table 5) and using the upper-limit S/Z equation from Hiley et~~

1004   ~~al. (2011) ($S = 0.21 \cdot \left(Z'\right)^{0.77}$; Sect. 1 and Eq. 1). The departures were evaluated as a relative~~

1005   ~~difference expressed as (S_{HP}-S)/S with S_{HP} one of four snowfall rates from Table 5. The relative~~

1006   ~~difference is no smaller than 0.7 and 1.0 on 15 December and 3 January, respectively. These~~

1007   ~~minimum relative differences exceed the hotplate precision (Sect. 2.4) by at least a factor of two.~~

1008   ~~It is concluded that our paired values of surface-measured precipitation rate and aircraft-~~

1009   ~~measured radar reflectivity, after correcting for attenuation, provide evidence that a calculation~~

1010   ~~of S based on the Hiley et al. (2011) upper-limit, when applied to rimed snow particles, is~~

1011   ~~associated with a low-biased estimate of S.~~

1012   ~~A plausible explanation~~ One plausible reason for the low bias discussed in the previous

1013   two paragraphs is the smaller density implicit in most computationally-based S/Z relationships

1014   and especially those which assume that snow particles are crystals. Densities are quite different

1015 for crystals versus that for rimed snow particles. For example, in Brown and Francis (1995),

1016 assuming a 2 mm crystal, the density is ~ 30 kg m^{-3}, whereas in PV11 (their Eq. 1), assuming a 2

1017 mm graupel particle, the density is ~ 200 kg m^{-3}. Because aggregates are collections of crystals,

1018 this comparison of crystal and graupel densities also seems relevant to a comparison of graupel

1019 and aggregate snow particle densities.

1020 ~~Fig. 12a~~ Figure 12 compares our S_{HP} / Z' data pairs to the SSKB S/Z relationship line

1021 ~~developed using density = 200 kg m^{-3} (Sect. 1).~~ and Table 1 presents the relative differences

1022 between the data pairs and the SSKB line. ~~also has the SSKB relationship. This was developed~~

1023 ~~using density = 200 kg m^{-3} (Sect. 1).~~ Compared to the S/Z relationship represented by top of the

1024 orange region in Fig. 12, and compared to the Matrosov 2007 relationship~~a~~, the SSKB line plots

1025 closer to our data points (minimum relative difference ~ 0.3). We note that the only instances of

1026 $S_{HP} < S$ are three of four comparisons of our measurements to the SSKB relationship. A possible

1027 reason for this is that the density applied in SSKB (Table 1) is not entirely representative of

1028 conditions during our study. An analysis of the sensitivity of the SSKB to a change in density is

1029 needed to investigate our assertion. ~~and closer to many of those reported by PV11.~~

1030 Comparisons of our S_{HP} / Z' data pairs and PV11's best-fit line are also in Table 1. The

1031 table demonstrates that the agreement is reasonable - minimum relative difference no larger than

1032 0.3 – and Fig. 12 shows that our data pairs plot at or above the PV11 best fit line.

1033 Based on data from PV11 and our S_{HP} / Z' data pairs~~result~~, as well as the S/Z relationship

1034 abbreviated SSKB ~~(Sect. 1)~~, it is expected that the S/Z relationships reported by Falconi et al.

1035 (2018) for rimed snow particles (Sect. 1) would plot higher in S-versus-Z space than is illustrated

1036 in Fig. 12~~b~~. Notably, only the upper-end of the Falconi et al. lines (i.e., at Z > 8 mm^6 m^{-3}) plot

1037 above the upper--limit that Hiley et al. (2011) developedestablished for unrimed snow particles.

1038 A plausible explanation for the lower-than-expected S/Z relationships of Falconi et al. is now

1039 offered. Falconi et al. used liquid water path as a proxy for the extent of snow particle riming

1040 (von Lerber et al. 2017). A consequence may have been that the proxy did not dependably

1041 exclude unrimed snow particles (crystals and aggregates) from the riming categories of Falconi

1042 et al. If this was the casetrue, then the data groupings that were the basis for the Falconi et al. S/Z

1043 relationships may have been affected. When applying the heavily-rimed S/Z relationship of

1044 Falconi et al. with our S_{HP}/Z' data pairs we find that the minimum relative differences are 0.6

1045 (December 15) and 8.5 (January 3) (Table 1). Additionally, the differences are 0.5 (December

1046 15) and 5.9 (January 3) when applying the moderately-rimed S/Z relationship of Falconi et al.

1047 (results not shown). Further research is needed to resolve the reason for the mismatch between

1048 S/Z pairs, the snowfall rate/reflectivity pairs reported both here and in PV11, here and the S/Z

1049 relationships reported in Falconi et al.

1050   Our conclusion that the upper-limit S/Z relationship from Hiley et al. (2011)

1051 underestimates S would be modified if our WCR-derived reflectivities were negatively biased.

1052 Assuming the reflectivities are negatively biased by 2.5 dBZ, the minimum relative differences

1053 discussed previously are no smaller than 0.1 and 0.3 on 15 December and 3 January,

1054 respectively. A bias in reflectivity of this magnitude cannot be ruled out but neither can a

1055 positive bias of the same magnitude (Sect. 2.3). The latter increases the minimum relative

1056 differences to 1.6 and 2.2 on 15 December and 3 January, respectively. In each of these

1057 calculations we have summed the attenuations (Table 43) with ± 2.5 dBZ and used Eq. 1 to

1058 calculate error-perturbed reflectivities.

1059   The scatter of measurements in Fig. 12a, the plausibility of a -2.5 to +2.5 dBZ bias in

1060   WCR reflectivity measurements, and error in measurement of S (Sect. 2.4), indicate that refined

1061   techniques will be needed in future investigations which apply the approach described here.

1062   Taking into consideration the goal of evaluating snowfall rates from space, some advance in

1063   satellite remote sensing also seems warranted. One issue is diagnosing where riming is occurring

1064   within clouds. Both lidars and radiometers can sense supercooled liquid water from space (e.g.,

1065   Battaglia and Panegrossi, 2020), and if combined with Doppler radars operating at multiple

1066   wavelengths, can diagnose precipitation attributable to rimed snow particles. Despite limitations

1067   of the multiple-wavelength Doppler method, for example in scenarios with vertical air speed

1068   comparable to and larger than particle fall speed (Vogl et al. 2022), the method has been

1069   validated in ground-based field studies (Kneifel et al. 2015; Mason et al. 2018). Technical

1070   challenges also remain for implementing the method from space (Battaglia et al.

1071   2020).Additionally, improved methods are needed to diagnose situations where riming is

1072   occurring within clouds. Both lidars and radiometers can sense supercooled liquid water from

1073   space (e.g., Battaglia and Panegrossi, 2020), and if combined with Doppler radar, can diagnose

1074   precipitation attributable to rimed snow particles. These approaches are being tested in ground-

1075   based field studies (Kneifel et al. 2015; Moisseev et al. 2017; Mason et al. 2018) but are most

1076   reliable in scenarios with the magnitude of vertical air speed smaller than particle fall speed.

1077   **5 - Conclusions**

1078   We have reported The reported measurements consist of surface measurements of S and

1079   near-surface measurements of Z. The latter came from overflights of a ground site, where a

1080   precipitation gauge was operated, and were acquired using an airborne W-band radar. The values

1081   of Z were corrected for attenuation.

1082   The reported ~~S/~~ S_{HP}/Z' ~~Z~~ pairs plot at or above the S-versus-Z best-fit line of PV11 (Fig.

1083   12) and the~~.~~ minimum relative S difference (Table 1) is no larger than 0.3~~However, the points do~~

1084   ~~not depart beyond the variability evident in a replotting of S/Z pairs from PV11~~. The PV11 data

1085   came from airborne measurements of W-band reflectivity, acquired within ± 100 m of flight

1086   level, and from coincident measurements of snow particle imagery. PV11 used a density-size

1087   function and a fall speed-size function, and measurements (PSD and particle images) to calculate

1088   S for snow particles that were classified as both rimed crystals and graupel. ~~.~~ This classification

1089   is also consistent with the particle imagery we have presented (Fig. 11).

1090   ~~There is a~~We have documented a substantial difference in comparisons~~n offset~~ between

1091   our ~~the~~ snowfall rates~~S points, reported here,~~ and reflectivity-dependent S values calculated~~ at~~

1092   using an upper-limit S/Z relationship for unrimed snow particles (Hiley et al. 2011). Here the

1093   minimum relative S differences are 0.7 and 1.0 for our two overflights and in a comparison to

1094   our measurements correspond to an underestimation of snowfall rate (Fig. 12). Th~~e~~e relative

1095   differences~~offset~~ are~~is~~ approximately a factor of two larger than the precision of our snowfall

1096   rate~~the S~~ measurement. We also report a substantial difference, and S underestimation compared

1097   to our measurements (Fig. 12), for the comparison made to an S/Z relationship which assumes

1098   the snow particles are aggregates (Matrosov 2007). The snowfall rate underestimates obtained

1099   using both Hiley et al.'s and Matrosov's S/Z relationships (Fig. 12) are perhaps expected given

1100   that the density factored into those S/Z calculations is small compared to that for rimed snow

1101   particles. It is also expected that the larger density and spherical shape applied in the SSKB S/Z

1102   relationship contributed to the better agreement (minimum relative difference ~ 0.3) with our

1103 S_{HP}/Z' pairs. Our conclusion is that some snowfall retrievals (e.g., Hiley et al. 2011) will

1104   underestimate S for weather targets containing rimed snow particles. We also state that our

conclusion is at odds with measurements and analysis in Falconi et al. Those researchers

reported S/Z relationships for rimed snow particles which in instances with $Z < 8$ mm^6 m^{-3} plot

below the upper-limit of Hiley et al. (Fig. 12). The consequence is that the minimum relative S

difference in our comparison to Falconi et al. (assuming Falconi et al.'s heavily-rimed

classification) is comparable to and larger than in our comparison to the Hiley et al.'s upper-limit

S/Z relationship.

~~This suggests that a measured Z and the Hiley et al. (2011) upper limit will produce an~~

~~underestimate of precipitation in scenarios dominated by rimed snow particles.~~

New research is needed to refine the S/Z relationship for rimed snow particles. This could

be computational – e.g., investigation of~~ing~~ the utility of parameterizing S in terms of both Z and

density – or could be observational. Unlike the investigation of PV11, where only an airborne

platform was employed, we have demonstrated that useful information can be obtained using

coordinated ground-based and airborne systems. Another approach would be with only ground-

based instrumentation. This would avoid some of the complications encountered in this study,

including W-band attenuation and a reliance on particle imagery acquired aloft. A study with

both ground-based and airborne systems would also be useful for understanding an S/Z

mismatch~~,~~ apparent at $Z < 8$ mm^6 m^{-3}~~; and which is larger than the offset summarized in the~~

~~previous paragraph.~~ Elements of the mismatch are ~~the S/Z measurements reported by PV11,~~ the

measurements reported here, PV11's best-fit line, and the measurement-based S/Z relationships

reported by Falconi et al. (2018). These three research teams reported measurements relevant to

the development of an S/Z relationship for rimed snow particles.

6 – Appendix

1127   This appendix explains how HP (hotplate) and WCR (Wyoming Cloud Radar) averages

1128   were evaluated. The scheme starts with an HP averaging interval (duration 60 s) and derives a

1129   WCR averaging interval and a WCR averaging domain. The latter encompasses a subset of the

1130   altitude-time crossection sampled by the WCR. The top boundary of the domain was derived

1131   using vertical-component Doppler velocities within the interval/domain. Because of this

1132   dependence, the line defining the top boundary ~~had to be~~ was derived iteratively.

1133   With the overflight time symbolized t_0, the beginning and ending times of ~~the first of~~ two

1134   60-second HP averaging intervals are

1135 $$t_{HP,B} = t_O \quad \cancel{t_{HP,B} = t_O} \tag{A1}$$

1136 $$t_{HP,E} = t_O + 60 \tag{A2}$$

1137   Since two adjacent HP averaging intervals are evaluated in this analysis, we express the

1138   averaging times with the following recursive equations

1139 $$t_{HP,B}(i) = t_O + i \cdot 60 \tag{A3}$$

1140   and

1141 $$t_{HP,E}(i) = t_O + (i+1) \cdot 60. \tag{A4}$$

1142   In Eqs. A3-A4 the index is $\cancel{i \in} i \in \{0, 1\}$. A special case with $i = 2$ is also analyzed (~~in~~ Sect.

1143   3.5)~~.~~~~;~~

1144   Analogous to the recursion in Eq. A4, the ending time of a WCR averaging interval is

1145 $$t_{WCR,E}(i) = t_O - i \cdot 60 \cdot v_w / gs. \tag{A5}$$

1146 Here v_w is a wind advection speed (discussed below) and the second term on the rhs is a wind

1147 advection distance divided by the WKA (Wyoming King Air) ground speed ($\cancel{gs}$ gs). Analogous

1148 to the Eq. A5, the beginning time of a WCR averaging interval is

1149 $$t_{WCR,B}(i) = t_{WCR,E} - (i+1) \cdot 60 \cdot v_w / gs \qquad (A6)$$

1150 The wind advection speed (v_w) in Eqs. A5-A6 was calculated using an altitude-

1151 dependent west-to-east wind velocity (u $\cancel{u}$) and an altitude-dependent south-to-north wind

1152 velocity (v $\cancel{v}$). These altitude-dependent component velocities were calculated using the

1153 horizontal wind vectors in the penultimate and last columns of Table 3$\cancel{2}$. Plots of the component

1154 velocities versus altitude and the linear functions used to relate component velocities to altitude

1155 are presented in Figs. A1a-b.

1156 An altitude (z' $\cancel{z}$= 3400 m) was assumed for evaluating the horizontal wind advection

1157 vector. This is the altitude of the ridges west and northwest of the HP site (Figs. 3a-b).

1158 The WKA track vector (Table 3$\cancel{2}$) defines the vertical plane of the WCR measurements.

1159 We assumed that wind advection of snow particles occurred parallel to this vector. With the

1160 assumption stated in the previous paragraph, the horizontal wind advection speed (v_w) was

1161 calculated as the projection of the horizontal wind vector onto the track vector.

1162 $$v_w = \frac{u(z') \cdot gs_x + v(z') \cdot gs_y}{\left(gs_x^2 + gs_y^2\right)^{1/2}} \qquad (A7)$$

1163 In Eq. A7 the west-to-east and south-to-north components of the track vector are symbolized gs_x

1164 and gs_y. Vector representations of the track vector are in Table 3$\cancel{2}$. On 14/15 December 2016 and

1165 3 January 2017, the values of v_w are 7.4 and 8.9 m s^{-1}, respectively.

1166   In addition to the properties gs ~~gs~~ and v_w used to evaluate Eqs. A5-A6, a WCR

1167   averaging interval/domain was evaluated using a snow particle downward speed (Eq. A8).

1168 $v_p = |<V_D>| + \sigma_{V_D}$ (A8)

1169   Here, $<V_D>$ is the average of Doppler velocities within an averaging interval/domain,

1170 $|<V_D>|$ is the absolute value of the average, and σ_{V_D} is the standard deviation of the average.

1171   On both the lhs and rhs of Eq. A8, all terms are greater than zero.

1172   We interpret v_p as the maximum likely snow particle speed toward the ground. There are

1173   three reasons for this: 1) For the WCR averaging intervals/domains we analyzed, values of

1174 $<V_D>$ were consistently less than zero (Table 6~~5~~). This indicates that snow particles (on

1175   average) were moving toward the ground. 2) Again, for the WCR averaging intervals/domains

1176   we analyzed, σ_{V_D} was comparable to $|<V_D>|$. This indicates that turbulent eddies transported

1177   snow particles upward and downward at a speed comparable their downward speed in still air. 3)

1178   The V_D are reflectivity weighted (Haimov and Rodi 2013) and are thus indicative of the motion

1179   of the largest particles within an averaging interval/domain.

1180   We now focus on the top boundary of a WCR averaging interval/domain. Figures 6b and

1181   6d have representations of the boundary. The slope defining this boundary was calculated as

1182 $-v_p \cdot gs / v_w$. That is, particles below this boundary moved downward sufficiently fast and

1183   horizontally sufficiently slow to advect reasonably close to the hotplate. Starting with diagnosed

1184   values of gs ~~gs~~ and v_w, the values of v_p and slope, were derived iteratively. The precision of the

1185   derived v_p is ± 0.1 m s^{-1}.
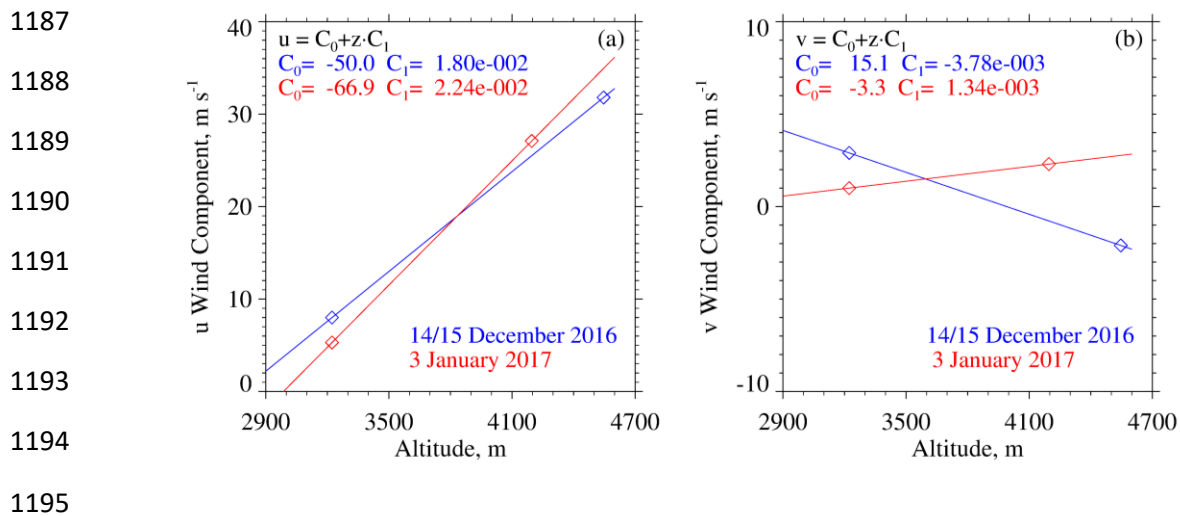
1186

Figure A1 – (a) West-to-east (u) wind velocity derived using measurements from the WKA

and the AmeriFlux (AF) tower. Also shown is the linear function used to relate u to altitude.

(b) South-to-north (v) wind velocity derived using measurements from the WKA and AF. Also

shown is the linear function used to relate v to altitude. WKA and AF velocities are presented

as vectors in the penultimate and last columns of Table 3.

1202   Data Availability. The WKA and WCR measurements can be obtained from the SNOWIE data

1203   archive of NCAR/EOL, which is sponsored by the National Science Foundation. Hotplate gauge

1204   measurements are at https://doi.org/10.15786/20103146. The US-GLE AmeriFlux measurements

1205   are at https://ameriflux.lbl.gov/. The Brooklyn Lake SNOTEL gauge measurements are at

1206   https://www.wcc.nrcs.usda.gov/snow/. Merged Hotplate, SNOTEL, and AmeriFlux data

1207   sequences from 14/15 December 2016 and 3 January 2017 are in Snider (2023).

1208

1209   Author contributions. JS and MB wrote the grant proposal that funded this research. Field

1210   measurements were performed by SF, SM, SH, MB, and JS. SF wrote her MS dissertation, and

1211   this was adapted for this paper by JS. KS processed the snow particle imagery. AM maintained

1212   the measurement sites. All authors contributed to the editing of this paper.

1213

1214 **Acknowledgements –**

1215   We acknowledge technical assistance provided by David Plummer, Larry Oolman, Zane

1216 Little, Brent Glover, Edward Sigel, Thomas Drew, and Brett Wadsworth. We thank SNOWIE

1217 project PI Jeffery French, who provided the flight data, Gabor Vali who provided the S/Z data

1218 points in Fig. 12a, and John Frank and John Korfmacher who acquired the GLE-US AmeriFlux

1219 data set. This work was supported by the United States National Science Foundation (Award

1220 Number 1850809) and the John P. Ellbogen Foundation.

1221

References

AmeriFlux, https://ameriflux.lbl.gov/, 2021

Battaglia, A. and Panegrossi, G., What Can We Learn from the CloudSat Radiometric Mode Observations of Snowfall over the Ice-Free Ocean?, 12, 3285, https://doi.org/10.3390/rs12203285, 2020

Battaglia, A., Tanelli, S., Tridon, F., Kneifel, S., Leinonen, J., and Kollias, P, Triple-Frequency Radar Retrievals, In: Levizzani, V., Kidd, C., Kirschbaum, D.B., Kummerow, C.D., Nakamura, K., Turk, F.J. (eds) *Satellite Precipitation Measurement*, Advances in Global Change Research, vol 67. Springer, Cham. https://doi.org/10.1007/978-3-030-24568-9_13, 2020

Boudala, F.S., R. Rasmussen, G.A. Isaac, and B. Scott, Performance of Hot Plate for Measuring Solid Precipitation in Complex Terrain during the 2010 Vancouver Winter Olympics, J. Atmos. Oceanic Technol., 31, 437–446, https://doi.org/10.1175/JTECH-D-12-00247.1, 2014

Braham , R. R., Snow Particle Size Spectra in Lake Effect Snows. J. Appl. Meteor. Climatol., 29, 200–207, https://doi.org/10.1175/1520-0450(1990)029<0200:SPSSIL>2.0.CO;2, 1990

Brock, F. V., and Richardson, S. J., Meteorological Measurement Systems, Oxford University Press, New York, 304 pp., 2001

Brown, P. R. A., and P. N. Francis, Improved Measurements of the Ice Water Content in Cirrus Using a Total-Water Probe. J. Atmos. Oceanic Technol., 12, 410–414, https://doi.org/10.1175/1520-0426(1995)012<0410:IMOTIW>2.0.CO;2., 1995

Cocks, S.B., S.M. Martinaitis, B. Kaney, J. Zhang, and K. Howard, MRMS QPE Performance during the 2013/14 Cool Season, J. Hydrometeor., 17, 791–810, https://doi.org/10.1175/JHM-D-15-0095.1, 2016

Faber, S., French, J. R., and Jackson, R., Laboratory and in-flight evaluation of measurement uncertainties from a commercial Cloud Droplet Probe (CDP), Atmos. Meas. Tech., 11, 3645–3659, https://doi.org/10.5194/amt-11-3645-2018, 2018

Falconi, M. T., von Lerber, A., Ori, D., Marzano, F. S., and Moisseev, D.: Snowfall retrieval at X, Ka and W bands: consistency of backscattering and microphysical properties using BAECC ground-based measurements, Atmos. Meas. Tech., 11, 3059–3079, https://doi.org/10.5194/amt-11-3059-2018, 2018

1250 Field, P.R., Hogan, R.J., Brown, P.R.A., Illingworth, A.J., Choularton, T.W. and Cotton, R.J.,
1251   Parametrization of ice-particle size distributions for mid-latitude stratiform cloud. Q.J.R. Meteorol.
1252   Soc., 131: 1997-2017. https://doi.org/10.1256/qj.04.134, 2005

1253 Fuller, S.E., Improvement of the Snowfall / Reflectivity Relationship for W-band Radars, MS Thesis,
1254   Department of Atmospheric Science, University of Wyoming, 2020

1255 Geerts, B., Q. Miao, Y. Yang, R. Rasmussen, and D. Breed, An Airborne Profiling Radar Study of the
1256   Impact of Glaciogenic Cloud Seeding on Snowfall from Winter Orographic Clouds, J. Atmos. Sci.,
1257   67, 3286–3302, https://doi.org/10.1175/2010JAS3496.1, 2010

1258 Haimov, S., and Rodi, A., Fixed-Antenna Pointing-Angle Calibration of Airborne Doppler Cloud Radar,
1259   Journal of Atmospheric and Oceanic Technology, 30, 2320-2335, https://doi.org/10.1175/JTECH-
1260   D-12-00262.1, 2013

1261 Hiley, M. J., M. S. Kulie, and R. Bennartz, Uncertainty Analysis for CloudSat Snowfall Retrievals, J. Appl.
1262   Meteor. Climatol., 50, 399–418, 2011

1263 Kneifel, S., von Lerber, A., Tiira, J., Moisseev, D., Kollias, P., and Leinonen, J., Observed relations between
1264   snowfall microphysics and triple-frequency radar measurements. J. Geophys. Res. Atmos., 120,
1265   6034– 6055, doi: 10.1002/2015JD023156, 2015

1266 Kochendorfer, J., Nitu, R., Wolff, M., Mekis, E., Rasmussen, R., Baker, B., and Jachcik, A, Testing and
1267   development of transfer functions for weighing precipitation gauges in WMO-SPICE, Hydrology
1268   and Earth System Sciences, 2, 1437-1452, https://doi.org/10.5194/hess-22-1437-2018, 2018

1269 Korolev, A. V., E. F. Emery, J. W. Strapp, S. G. Cober, G. A. Isaac, M. Wasey, and D. Marcotte, Small ice
1270   particles in tropospheric clouds: Fact or artifact? Airborne Icing Instrumentation Evaluation
1271   Experiment, Bull. Amer. Meteor. Soc., 92, 967–973, https://doi.org/10.1175/2010BAMS3141.1,
1272   2011

1273 Kulie, M. S., and R. Bennartz, Utilizing Spaceborne Radars to Retrieve Dry Snowfall, J. Appl. Meteor.
1274   Climatol., 48, 2564–2580, https://doi.org/10.1175/2009JAMC2193.1, 2009

1275 Kulie, M. S., Milani, L., Wood, N. B., Tushaus, S. A., Bennartz, R., and L'Ecuyer, T. S., A Shallow
1276   Cumuliform Snowfall Census Using Spaceborne Radar, Journal of Hydrometeorology, 4, 1261-
1277   1279, https://doi.org/10.1175/JHM-D-15-0123.1, 2016

1278 Lawson, R. P., O'Connor, D., Zmarzly, P., Weaver, K., Baker, B., Mo, Q., and Jonsson, H., The 2D-S
1279   (Stereo) Probe: Design and Preliminary Tests of a New Airborne, High-Speed, High-Resolution

1280   Particle Imaging Probe, J. Atmos. Ocean. Tech., 23, 1462–1477,
1281   https://doi.org/10.1175/JTECH1927.1, 2006

1282 Liebe, H.J., Manabe, T., and Hufford, G.A., Millimeter–wave attenuation and delay rates due fog/cloud
1283   conditions, IEEE Trans. Antenn. Propag., 37, 1617–1623, 1989

1284 Liu, C.-L., and A. J. Illingworth, Toward more accurate retrievals of ice water content from radar
1285   measurements of clouds, J. Appl. Meteor., 39, 1130–1146, 2000

1286 Locatelli, J.D. and Hobbs, P.V., Fall speed and masses of solid precipitation particles, J. Geophys. Res., 79,
1287   2185–2197, https://doi.org/10.1029/JC079i015p02185, 1974

1288 Macklin, W.C., The density and structure of ice formed by accretion, Q.J.R.Meteorol.Soc., 88: 30-50.
1289   doi:10.1002/qj.49708837504, https://doi.org/10.1002/qj.49708837504, 1962

1290 Marlow, S.A, J.M. Frank, M. Burkhart, B. Borkhuu, S.E. Fuller, and J.R. Snider, Snowfall Measurements
1291   at Wind-exposed and Sheltered Sites in the Rocky Mountains of Southeastern Wyoming, in
1292   revision for the Journal of Applied Meteorology and Climatology, http://www-
1293   das.uwyo.edu/~jsnider/manuscript_revision2.docx, 2023

1294 Martinaitis, S.M., S.B. Cocks, Y. Qi, B.T. Kaney, J. Zhang, and K. Howard, Understanding winter
1295   precipitation impacts on automated gauge observations within a real-rime system, J. Hydrometeor.,
1296   16, 2345-2363, https://doi.org/10.1175/JHM-D-15-0020.1, 2015

1297 Mason, S. L., Chiu, C. J., Hogan, R. J., Moisseev, D., and Kneifel, S., Retrievals of riming and snow density
1298   from vertically pointing Doppler radars, Journal of Geophysical Research: Atmospheres, 123,
1299   13,807– 13,834, https://doi.org/10.1029/2018JD028603, 2018

1300 Matrosov, S.Y., Modeling Backscatter Properties of Snowfall at Millimeter Wavelengths, J. Atmos. Sci.,
1301   64, 1727-1736, https://doi.org/10.1175/JAS3904.1, 2007

1302 ~~Moisseev, D., von Lerber, A., and Tiira, J., Quantifying the effect of riming on snowfall using ground-~~
1303   ~~based observations, J. Geophys. Res. Atmos., 122, 4019–4037, doi:10.1002/2016JD026272, 2017~~

1304 Nemarich, J., Wellman, R.J., and Lacombe, J., Backscatter and attenuation by falling snow and rain at 96,
1305   140, and 225 GHz, IEEE Trans. Geosci. Remote, 26, 319–329, 1988

1306 Panofsky, H.A. and Dutton, J.A., *Atmospheric Turbulence*, Wiley-Interscience, New York, 397 pp., 1984

1307 Pokharel, B. and G. Vali, Evaluation of Collocated Measurements of Radar Reflectivity and Particle Sizes
1308   in Ice Clouds, J. Appl. Meteor. Climatol., 50, 2104–2119, https://doi.org/10.1175/JAMC-D-
1309   1005010.1, 2011

1310 Rasmussen, R.M., J. Hallett, R. Purcell, S.D. Landolt, and J. Cole, The Hotplate precipitation gauge, J.
1311   Atmos. Oceanic Technol., 28, 148-164, https://doi.org/10.1175/2010JTECHA1375.1, 2011

1312 R.M. Young Company, Model 05103 Wind Monitor, 2001

1313 Skofronick-Jackson, G., and Coauthors, The Global Precipitation Measurement (GPM)   Mission   for
1314   science and society, Bull. Amer. Meteor. Soc., 98, 1679–1695, https://doi.org/10.1175/BAMS-D-
1315   15-00306.1, 2017

1316 Smith, P.L., Equivalent radar reflectivity factors for snow and ice particles, J. Climatol. Appl. Meteor., 23,
1317   1258–1260, https://doi.org/10.1175/1520-0450(1984)023<1258:ERRFFS>2.0.CO;2, 1984

1318 Snider, J.R., Supplemental dataset for Marlow et al. (2023), https://doi.org/10.15786/20247870, 2023

1319 Surussavadee, C., and D. H. Staelin, Millimeter-Wave Precipitation Retrievals and Observed-versus-
1320   Simulated Radiance Distributions: Sensitivity to Assumptions. J. Atmos. Sci., 64, 3808–3826,
1321   https://doi.org/10.1175/2006JAS2045.1, 2007

1322 Tessendorf, S. A., and Coauthors, A transformational approach to winter orographic weather modification
1323   research: The SNOWIE Project, Bulletin of the American Meteorological Society, 100, 71–92,
1324   https://doi.org/10.1175/BAMS-D-17-0152.1, 2019

1325 Ulaby, F.T., Moore, R.K., and Fung, K., Microwave Remote Sensing: Active and Passive, Vol. 1,
1326   Microwave Remote Sensing Fundamentals and Radiometry, ARTECH HOUSE Inc., Norwood,
1327   MA, p. 456., 1981

1328 Vali, G. and Haimov, S., Observed extinction by clouds at 95 GHz, IEEE Trans. Geosci. Remote, 39, 190–
1329   193, 2001

1330 Vogl, T., Maahn, M., Kneifel, S., Schimmel, W., Moisseev, D., and Kalesse-Los, H.: Using artificial neural
1331   networks to predict riming from Doppler cloud radar observations, Atmos. Meas. Tech., 15, 365–
1332   381, https://doi.org/10.5194/amt-15-365-2022, 2022

1333 von Lerber, A., D. Moisseev, L. F. Bliven, W. Petersen, A. Harri, and V. Chandrasekar: Microphysical
1334   Properties of Snow and Their Link to Ze–S Relations during BAECC 2014. J. Appl. Meteor.
1335   Climatol., 56, 1561–1582, https://doi.org/10.1175/JAMC-D-16-0379.1, 2017

1336 Wang,Y., G.Liu, E.Seo, and Y.Fu, Liquid water in snowing clouds: Implications for satellite remote

1337 sensing of snowfall, Atmos. Res., 60-72, 10.1016/j.atmosres.2012.06.008, 2013

1338 Wang, P.K., and W. Ji, Collision Efficiencies of Ice Crystals at Low–Intermediate Reynolds Numbers

1339   Colliding with Supercooled Cloud Droplets: A Numerical Study, Journal of the Atmospheric

1340   Sciences, 57, 1001-1009, https://doi.org/10.1175/1520-0469(2000)057<1001:CEOICA>2.0.CO;2,

1341   2000

1342 Wilson, J., and E. Brandes, Radar measurement of rainfall—A summary, Bull. Amer. Meteor. Soc., 60,

1343   1048–1058, https://doi.org/10.1175/1520-0477(1979)060<1048:RMORS>2.0.CO;2, 1979

1344 Wolfe, J.P., and J.R. Snider, A relationship between reflectivity and snow rate for a high-altitude S-band

1345   radar, J. Appl. Meteor. Climatol., 51, 1111–1128, https://doi.org/10.1175/JAMC-D-11-0112.1,

1346   2012

1347 Zaremba, T.J., and Coauthors, Vertical motions in orographic cloud systems over the Payette River Basin.

1348   Part 1: Recovery of vertical motions and their uncertainty from airborne Doppler radial Velocity

1349   Measurements, in press at the Journal of Applied Meteorology and Climatology,

1350   https://doi.org/10.1175/JAMC-D-21-0228.1, 2022

1351 Zelasko, N., Wettlaufer, A., Borkhuu, B., Burkhart, M., Campbell, L. S., Steenburgh, W. J., and Snider,

1352   J.R., Hotplate precipitation gauge calibrations and field measurements, Atmos. Meas. Tech., 11,

1353   441-458, https://doi.org/10.5194/amt-11-441-2018, 2018

1354 Zikmunda, J. and Vali, G., Fall patterns and fall velocities of rimed ice crystals, J. Atmos. Sci., 29, 1334–

1355   1347, https://doi.org/10.1175/1520-0469(1972)029<1334:FPAFVO>2.0.CO;2, 1972

1356